POSITION SENSORLESS CONTROL OF A MAGNETICALLY LEVITATED (MAGLEV) SYSTEM

by

ESTEBAN RICARDO NOBOA

Presented to the Faculty of the Graduate School of

The University of Texas at Arlington in Partial Fulfillment

of the Requirements

for the Degree of

DOCTOR OF PHILOSOPHY

THE UNIVERSITY OF TEXAS AT ARLINGTON

AUGUST 2010

DEDICATION

To my beloved wife and daughter, and to my always remembered parents and brothers. They are indeed the center of my existence.

ACKNOWLEDGEMENTS

I would like to express my most sincere gratitude to my advisor Dr. Babak Fahimi for his guidance and words of wisdom throughout the course of this research.

The completion of this work and my education would have not been possible without the support, sacrifice and love of my wife and family. They have played a central role in my life and have always been an endless source of inspiration and motivation.

August 11, 2010

ABSTRACT

POSITION SENSORLESS CONTROL OF A

MAGNETICALLY LEVITATED

(MAGLEV) SYSTEM

Esteban R. Noboa, PhD.

The University of Texas at Arlington, 2010

Supervising Professor: Babak Fahimi

The main focus of this investigation is the development and implementation of a sensorless position estimation method and hysteresis position controller for a laboratory–based Maglev system. The proposed estimation method and controller are first validated through modeling and simulation. This sensorless scheme makes use of the maglev system's magnetic signature, namely, its inductance and requires only active phase current measurements. These measurements are then used along with the phase voltage equation to estimate position information that is in a one-to-one correspondence with the system's inductance. The theoretical aspects of the sensorless scheme are described. Finite element analysis (FEA) as well as experimental measurements have been carried out to obtain static and dynamics characteristics of the system. The proposed sensorless

method has been implemented on a DSP microcontroller and the experimental results of this implementation are presented. In addition, simulation results will show the feasibility and effectiveness of this model-based position estimation scheme.

TABLE OF CONTENTS

LIST OF FIGURES

LIST OF TABLES

CHAPTER 1

INTRODUCTION

Levitation is defined as the stable equilibrium of a body without contact with the earth. There are several ways to accomplish this equilibrium, but in magnetic levitation the forces that counteract gravity are produced by magnetic fields. These magnetic fields originate from permanent magnets or electric currents.

The use of magnetically levitated (maglev) systems has been increasingly gaining attention in a broad range of applications. As a means of ground transportation, maglev systems have been explored for the development of low and high speed trains. Other application areas of this technology are vibration isolation [1], magnetic bearings [2], nanopositioning devices [3], and recently NASA's Magnetic Launch Assist program is developing a maglev launching system that promises to reduce costs, increase reliability and lower the amount of pollution expended into the atmosphere [4].

In modern days, where the search for new environmentally friendly sources of energy and technologies is at its height, maglev offers a series of advantages over conventional transportation namely,

- Petroleum independence with respect to air and ground transportation.
- Less polluting as compared with air and ground vehicles.
- Faster trips. High speeds and high acceleration and braking allow for lower door-to-door trip time than conventional rail road systems.

- Higher passenger capacity than aircrafts. It also provides sufficient capacity to accommodate traffic growth.
- Convenience due to high frequency of service and the ability to serve.
- Improved comfort with respect to aircraft due to greater roominess.
- High reliability, less susceptible to congestions and weather conditions than air and ground vehicles.
- Acceptable safety, both perceived and actual based on foreign experience.

1.1 Historical Background

The modern development of magnetic levitation transportation systems started in the late 1960's as a natural consequence of the development of low-temperature superconducting wire [13]. Japan and Germany were the first countries to develop this technology for marketing. By mid-1980's both countries had test tracks built and functional and in 1996 Japan started public operation of its first line between Sakaigawa and Akiyama.

At the same time Germany started testing its Transrapid 07 maglev at the Transrapid Versuchanlage im Emsland test track (figure 1-1). By December 1996 their test vehicles had traveled more than 400,000 Km and had reached speeds over 400 Km/h. The German Transrapid is undergoing extensive testing and research in all aspects of the technology, i.e., materials, track design, etc. with the aim at making maglev transportation more marketable.

In China the Shanghai Transrapid (figure 1-2) was open to the public in 2004 with speeds of up to 430 Km/h. This line covers 30 miles from downtown Shanghai to the airport in about 6 to 8 minutes.

Figure 1-1 The German Transrapid 09

In 1990, the United States Federal Government and the Federal Railroad Administration began the National Maglev initiative. The purpose of this initiative was to evaluate methods of improvements for intercity transportation with maglev technology and to determine the role of the Federal government in the development of maglev systems. Regardless of all research on maglev technology that has been carried out, Federal authorities still are reluctant in investing in it. This resistance is due in part to the tradition that railroad systems have in the country.

Figure 1-2 The Shanghai Transrapid

1.2 State-of-the-art and literature review

Among the system configurations used in maglev applications are:

- Permanent Magnets
- Diamagnetic materials in a magnetic field
- Electromagnets
- Eddy currents
- Superconductors and permanent magnets
- Superconductors and superconducting magnets
- Hybrids, i.e., permanent magnets and electromagnets.

In maglev transportation there are two principal methods for magnetically levitating vehicles. The first method, called electromagnetic levitation (EML), uses attracting magnetic forces produced by non-superconducting electromagnets. The second

method, called electrodynamic levitation (EDL), employs repulsive forces between large superconducting magnets on the vehicle and eddy currents generated in a conducting track below the vehicle [13]. EDL and EML refer to the way the main actuator in a maglev system (magnet or electromagnet) and a guideway interact in levitating a body. Figures 1-3 to 1-5 show the most common geometrical arrangements in which the source of magnetic field and the guideway are set up.

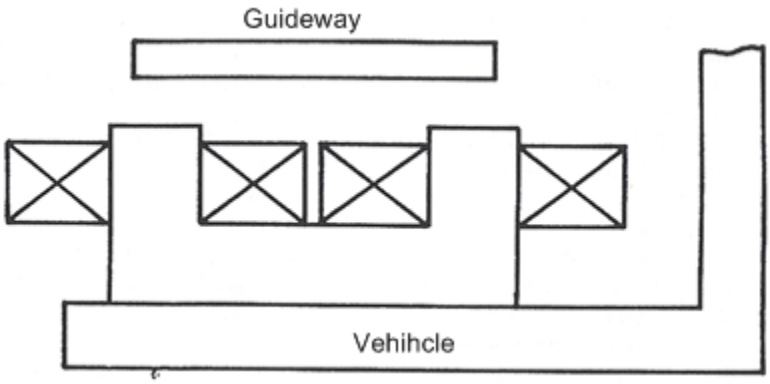

Figure 1-3 Electromagnet with shorter guideway width

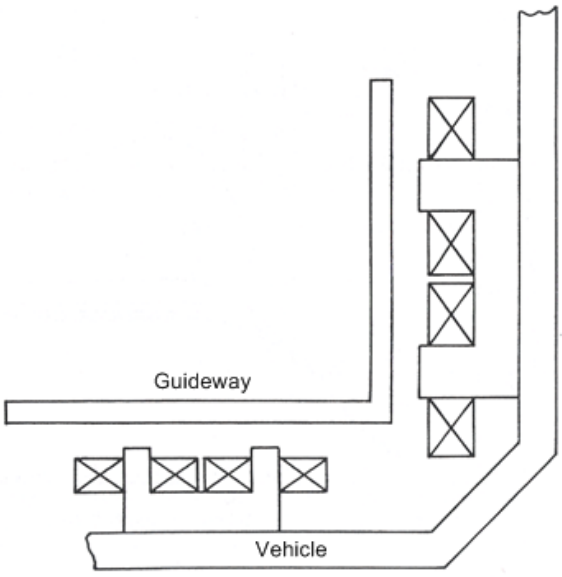

Figure 1-4 Separate electromagnets for guidance and suspension

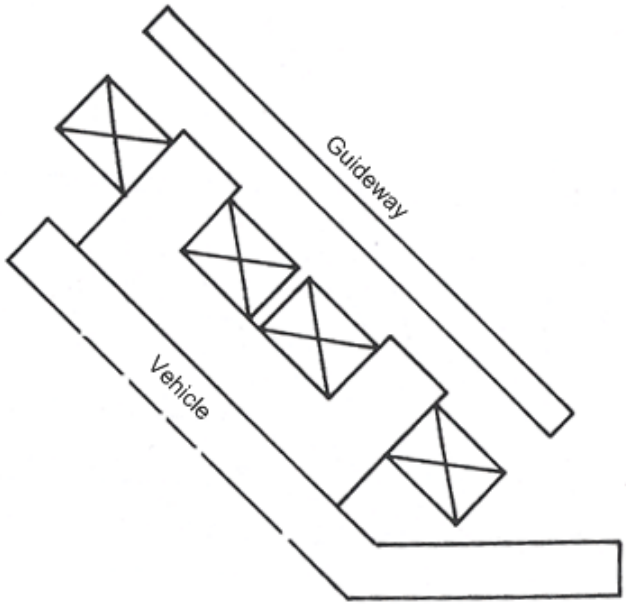

Figure 1-5 Single electromagnet with inclined guideway geometry

These configurations can broadly be classified into two groups: separate lift and guidance, and combined lift and guidance. The main advantage of the first group is the orthogonality of the two magnetic planes which allows independent control of the vertical and lateral dynamics. However, this arrangement needs an additional track for the guidance magnets. On the other hand, the combined structure provides savings in guideway cost at the expense of more complex controller structures.

With the advent of all these new maglev applications also comes the need for control strategies that enable the implementation of this technology in industry. Among the proposed control solutions are feedback linearization (both input-state and input-output) [5-7], sliding mode control [8] and also computing intensive techniques like Neural Networks [9] and Fuzzy Logic control [10]. However, these techniques rely on the availability of information about the entire system's state. Some work has been done

to obtain estimates of the states by means of a Luenberger observer [11] or a Kalman Filter [12].

1.3 Motivation

Designers of controllers for maglev systems face different challenges namely, highly nonlinear dynamics, unstable plants, and more than often these systems operate in harsh environmental conditions. But, controller design solves only one part of the problem, the other part is to count with reliable, accurate and timely information about the plant status. Regardless of the approach taken for control design, i.e., linear or nonlinear, the system state is always assumed to be available. In the case of nonlinear controllers, the entire system state is used to realize these controllers. This information is either directly measure with sensors or estimated from sensor measurements. In most common maglev applications measurements of position, velocity, acceleration and sometimes flux density are used for controller realization. The use of this extra hardware contributes to

Unreliability

Additional cost

Increase in system bulk

This thesis introduces a new position sensorless approach for the suspension of a maglev system. The reliability and in some other scenarios the survivability of a maglev system can be significantly improved by the implementation of a fall-back strategy that a sensorless control realization can offer.

1.4 Technical objectives

Specific goals of this work have been:

- Set up a model of an iron-core maglev electromechanical suspension for use in a laboratory environment.
- Static characterization of the maglev system with the use of FEA methods
- Development and analysis of the maglev dynamical model
- Design of a position controller for the maglev system
- Development and implementation of a sensorless airgap estimation technique using magnetic signatures of the maglev and its relation with position.
- Verification of static and dynamic models with experimental measurements.

1.5 Technical approach

In order to achieve the aforementioned goals, the static as well as dynamic characteristics of the maglev systems are studied first. This study is carried out through the development of a static FEA model. This model provides all magnetostatic properties of the maglev necessary to understand how the magnetic signature of this system relates to position of the levitated object. A Simulink® model was developed to gain insights on system dynamics. This model is useful in studying controller performance and selection of some hardware parameters. Also, the suitability of the sensorless scheme can be evaluated with this model as well as some implementation related issues.

The sensroless method is then implemented on a TMS320F2812 DSP controller and experimental measurements are taken and compared to analytical results.

CHAPTER 2

MAGLEV SYSTEM MODELING

In this chapter the analytical model of the maglev system is first derived using Ampere's law and the maglev equivalent magnetic circuit. A finite element model is then used to study the static characteristics of the maglev, namely, its magnetic force, flux density distribution and system inductance. This last characteristic and its relation to the levitated object's position are of particular interest to the implementation of the sensorless method. Simulink® is used for the implementation of the analytical equations and simulation results are presented. Stability considerations of the maglev closed loop control are also covered in this chapter and finally simulation results are discussed and compared.

2.1 Maglev analytical modeling using magnetic equivalent circuit

This section looks at the magnetic characteristics of the maglev and aims at finding an expression for the magnetic flux density B in the air gap and the flux linkage λ in the coils. These two quantities are necessary to develop a dynamic analytical model which is described in section 2.4. The magnetic model can be realized by considering Ampere's law around the contour shown in figure 2-2. Following this contour it is seen that the magnetic flux in this circuit is mainly determined by the permanent magnets and air gap characteristics.

Permanent magnets characteristics are usually described by their demagnetization curve. This demagnetization curve, also known as normal curve, represents the total magnetic flux that is carried in combination by the air and the PM. This curve is plotted in the second quadrant of a B-H coordinate system where PMs normally operate. A typical demagnetization curve is shown in figure 2-1. The load line, also shown in figure 2-1, provides the amount of flux density produce by a PM in a system with a particular geometry and material characteristics. But this production of flux density must be bounded by the PM characteristics and therefore the actual operating point is given by the intersection of the load line and the demagnetization line.

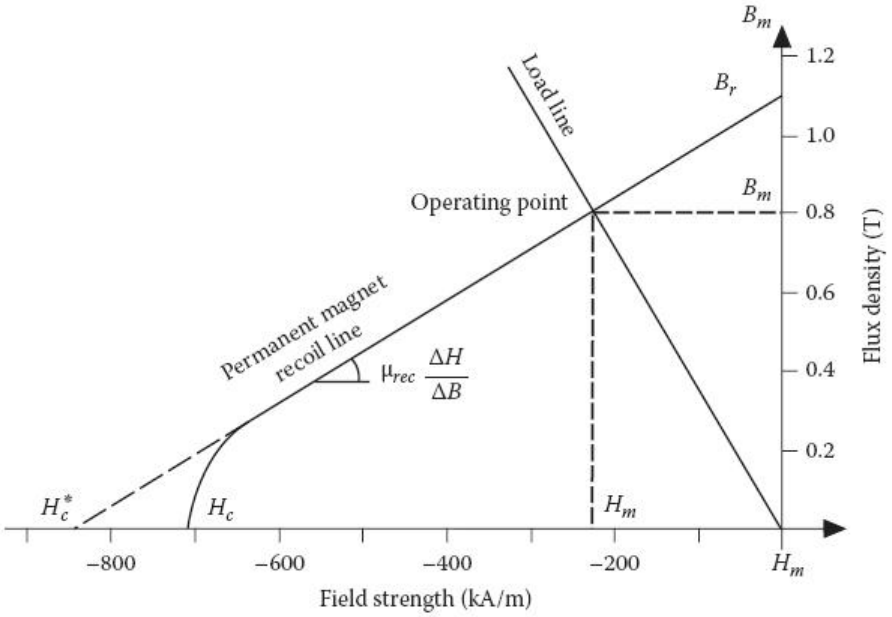

Figure 2-1 Permanent magnet demagnetization curve

The application of Ampere's Law to the contour shown in figure 2-2 provides a means to modeling of PMs. Considering only the PMs in the magnetic circuit of figure 2-2, Ampere's law gives

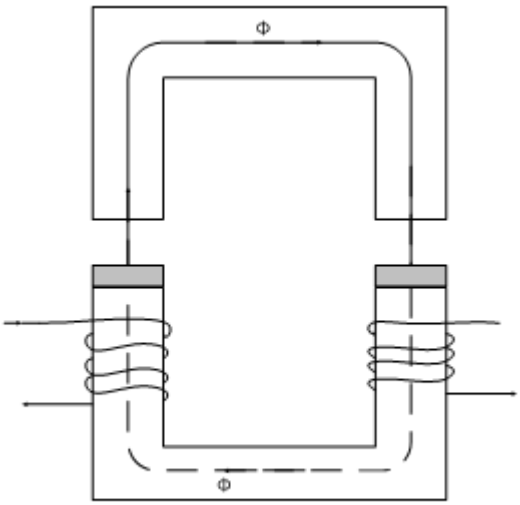

Figure 2-2 Maglev magnetic circuit

$$H_m L_m + H_{Ag} L_{Ag} = 0 \tag{2.1}$$

Where H_m and H_{Ag} are the magnetic field strength of the PM and air gap, respectively. Also,

$$\emptyset = B_m A_m = B_{Ag} A_{Ag} \tag{2.1.a}$$

Where B_m, B_{Ag}, A_m and A_{Ag} are the flux density in the PM, flux density in the air gap, cross-sectional area of the PM and cross-sectional area of the air gap respectively. Consideration of the constitutive equation of air $B_{Ag} = \mu_0 H_{Ag}$ and equation (2.5.a), yields

$$H_m L_m + B_m \frac{A_m L_{Ag}}{\mu_0 A_{Ag}} = 0 \tag{2.2}$$

$$B_m = -\left(\mu_0 \frac{A_{Ag} L_m}{A_m L_{Ag}}\right) H_m \tag{2.2.a}$$

Where L_{Ag} and L_M are the air gap length (also called x) and permanent magnets thickness respectively. Equation (2.2.a) represents the load line of figure 2-1. The demagnetization curve can be expressed as

$$B_m = \mu_r \mu_0 H_m + B_r \tag{2.3}$$

Where B_r and H_c are the PM retentivity and coercive force respectively, and $\mu_0 = 4\pi \times 10^{-7}$ H/m is the permeability of free space. Using equations (2.2.a) and (2.3) to find the intersection between the demagnetization and load lines gives,

$$B_m = B_r \left(\frac{1}{1 + \left(\frac{L_{Ag}}{\mu_0 A_{Ag}}\right)\left(\frac{\mu_r \mu_0 A_m}{L_m}\right)} \right) \tag{2.4}$$

If $R_m = L_m/(\mu_r A_m)$ and $R_{Ag} = L_{Ag}/(\mu_r \mu_0 A_{Ag})$, then (2.4) can be written as

$$B_m = B_r \left(\frac{1}{1 + \frac{R_{Ag}}{R_m}} \right) \tag{2.5}$$

$$B_m = B_r \left(\frac{R_m}{R_{Ag} + R_m} \right) \tag{2.5.a}$$

$$\emptyset_m = \emptyset_r \left(\frac{R_m}{R_{Ag} + R_m} \right) \tag{2.5.b}$$

The equivalent magnetic network is shown in figure 2-3. The PM is represented by the residual flux generator $\Phi_r = B_r A_m$ in parallel with the reluctance R_m [14].

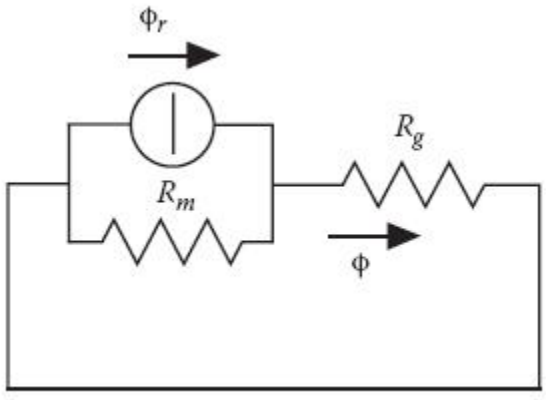

Figure 2-3 PM equivalent network

The maglev equivalent magnetic circuit is shown in figure 2-4. The application of Ampere's Law to this magnetic circuit will provide a means to find λ. Ampere law is written as

$$2H_M L_M + 2H_{Ag} L_{Ag} = 2NI \tag{2.6}$$

And the load line is now,

$$B_m = -\left(\frac{\mu_0 L_m A_{Ag}}{L_{Ag} A_m}\right) H_m + \left(\frac{\mu_0 A_{Ag} N}{A_m L_{Ag}}\right) I \tag{2.7}$$

The load line moves along the H_m axis a quantity ΔH_i proportional to the coil current, as shown in figure 2-5 [14].

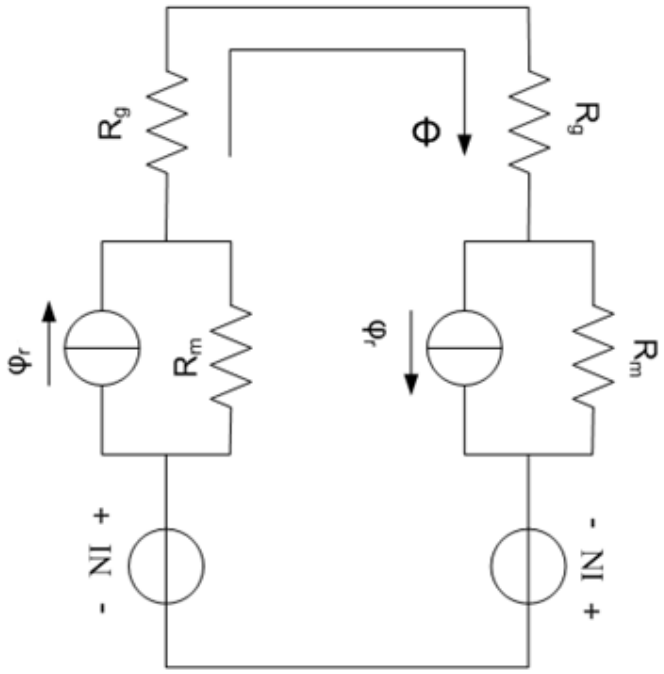

Figure 2-4 Maglev equivalent magnetic circuit

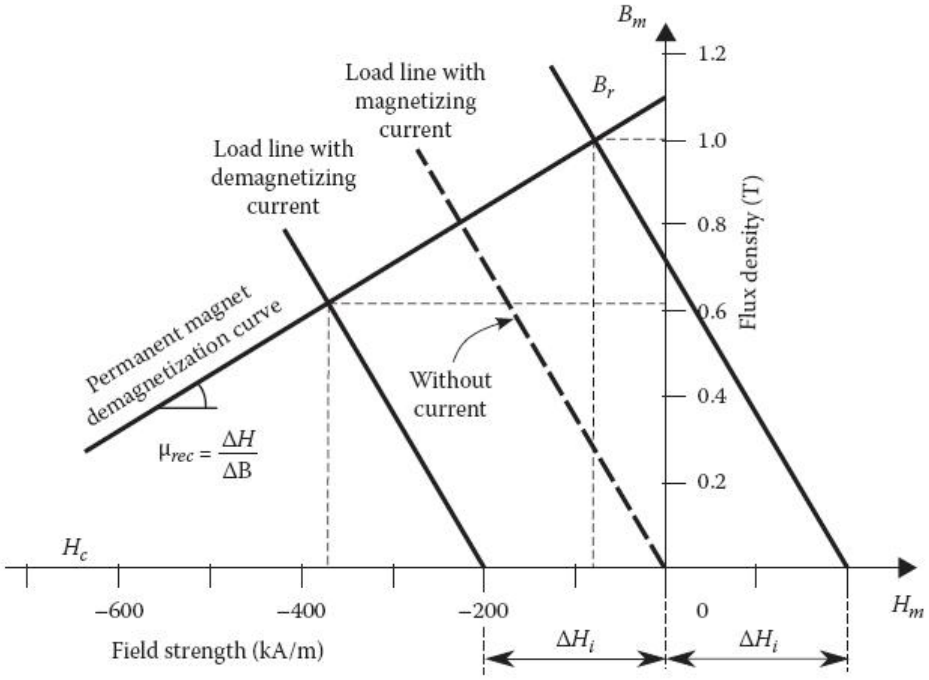

Figure 2-5 PM operating point with current

When a magnetizing current is applied, the line moves in the direction of positive magnetic fields. A demagnetizing current will cause a translation of the line in the opposite direction and, if large enough, could move the operating point beyond the linear region of the demagnetization curve. An excessively large current in this direction could irreversibly demagnetize the PM.

Combination of equations (2.3) and (2.7) gives the PM operating point in the presence of coil current.

$$B_m = \frac{NI + H_c L_M}{\frac{x}{\mu_0}\frac{A_m}{A_{Ag}} + \frac{H_c L_M}{B_r}} \tag{2.8}$$

The numerator of this equation shows the contribution of the electromagnet current as well as the permanent magnets to the flux density. This expression is fundamental to

finding the attracting magnetic force and the flux linkage λ in the coils. B_m and λ in the coils are related by:

$$\lambda = 2NA_m B_m \tag{2.9}$$

Where N is the number of coil turns. The magnetic force can be found by considering the magnetic energy stored in the air gap per unit of volume (Energy density):

$$E_{density} = \frac{1}{2} B_{Ag} H_{Ag} \tag{2.10}$$

$$E_{density} = \frac{1}{2\mu_0} {B_{Ag}}^2 \tag{2.10.a}$$

The magnetic force can be found as the energy stored per unit of length:

$$F_M = \frac{E_{density}}{L} A_{Ag} L \tag{2.11}$$

$$F_M = \frac{A_{Ag}}{2\mu_0} {B_{Ag}}^2 \tag{2.11.a}$$

Substitution of equation (2.11.a) in equation (2.8) finally gives an expression for the magnetic force:

$$F_M = \mu_0 A_{Ag} \left[\frac{Ni + H_c L_m}{x + \mu_0 A_{Ag} R_m} \right]^2 \tag{2.12}$$

$$F_M = \mu_0 A_{Ag} \left[\frac{Ni + K_1}{x + \mu_0 A_{Ag} R_m} \right]^2 \tag{2.12.a}$$

Where $K_1 = H_c L_m$. This expression of the magnetic force will be used in section 2.4 in the development of the dynamic model of the maglev system. Equations (2.12.a), (2.8) and (2.9) can be used to develop an analytical model.

2.2 Maglev Finite Element Model

A 2D - magnetostatic model of the maglev system was developed with Magnet® from Infolytica. Among the static characteristics obtained with this model are the magnetic force, inductance, flux linkage and flux density. The model was also used to ensure an operating point without saturation effects in the rotor and stator cores. The 2D geometry of the model, shown in figure 2.6, comprises the following parts: stator, rotor, permanent magnets and coils. The different materials used in this model are listed in table 2.1. An important parameter in any FEA model is the number of mesh elements. More than often the number of elements must be increased especially in the surface area of interest. In the maglev model this area is the air gap between rotor and stator, shown in figure 2.7, where an increase of uniform mesh elements is necessary for better accuracy.

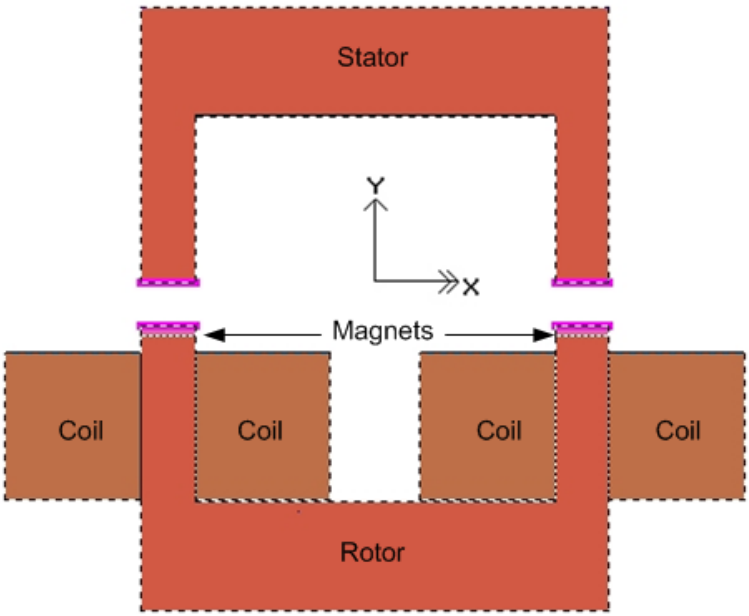

Figure 2-6 Magnet FEA model of maglev

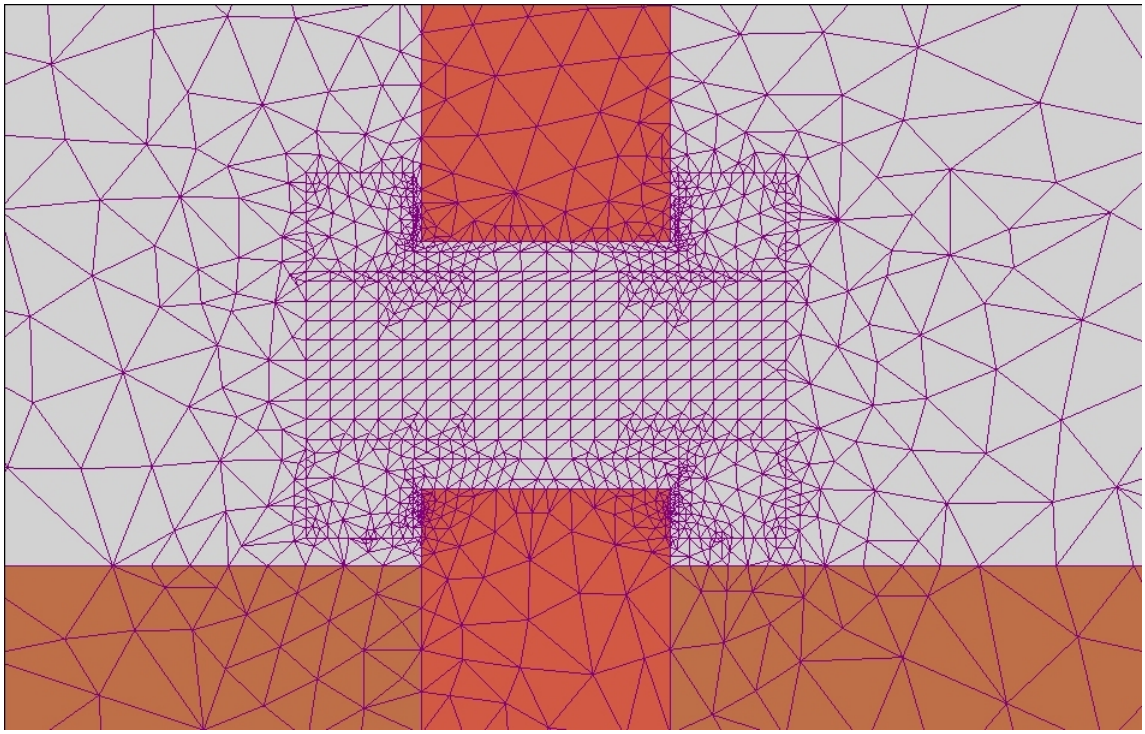

Figure 2-7 Maglev air gap mesh

Table 2-1 Material list for the Maglev FEA model

Model Object	Material
Core (stator and rotor)	M19 (72-29 gage)
Permanent Magnets	Neodymiun Iron Boron (NdFeB30)
Coils	Copper (stranded)

The FEA model was useful in determining the maximum reference current in the hysteresis band. Several simulations were performed to ensure operation in the linear region of the core *B-H* curve. For M19 the saturation region starts at approximately B = 1.1T. The values of coil currents that allow linear operation were then used with the Simulink® model to verify proper controller operation. It was observed that this maximum current value cannot exceed 0.65A. Larger values of current will cause very

fast rotor dynamics with an excessively large attraction force between rotor and stator that cannot be counteracted by the smallest positive coil current. A negative coil current is not an option in this case since magnets demagnetization must be avoided. This limitation imposes a boundary on the maglev payload.

2.3 Static characteristics of Maglev system

FEA analysis is useful in finding the range of variation of static quantities like force, inductance and magnetic flux density. This information is crucial in determining the system magnetic status under different operating conditions. Figure 2-8 shows the flux density distribution when the air gap is 5mm and the coil current is 0.65A. It is seen that the maximum B is less than 0.65T and occurs in the inner corners of the cores, which guarantees a linear operation.

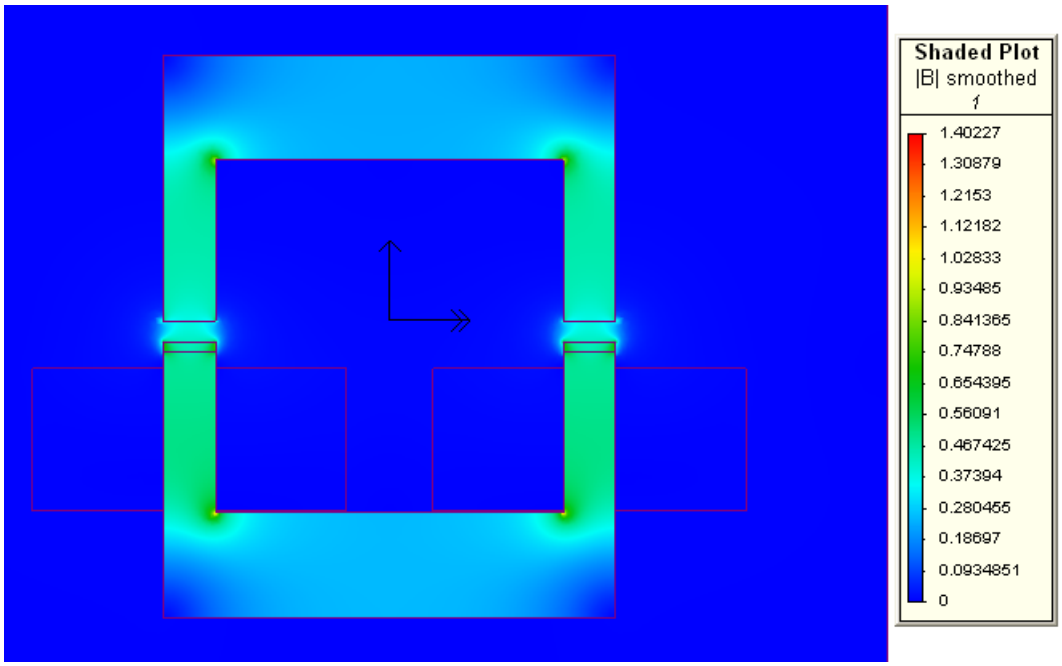

Figure 2-8 Maglev Flux Density distribution

Another representation of flux density is depicted in figure 2-9 where values of *B* have been plotted along a horizontal sweep. This picture shows that the maximum value of *B*, which occurs in the narrow parts of the core, is approximately 0.45T.

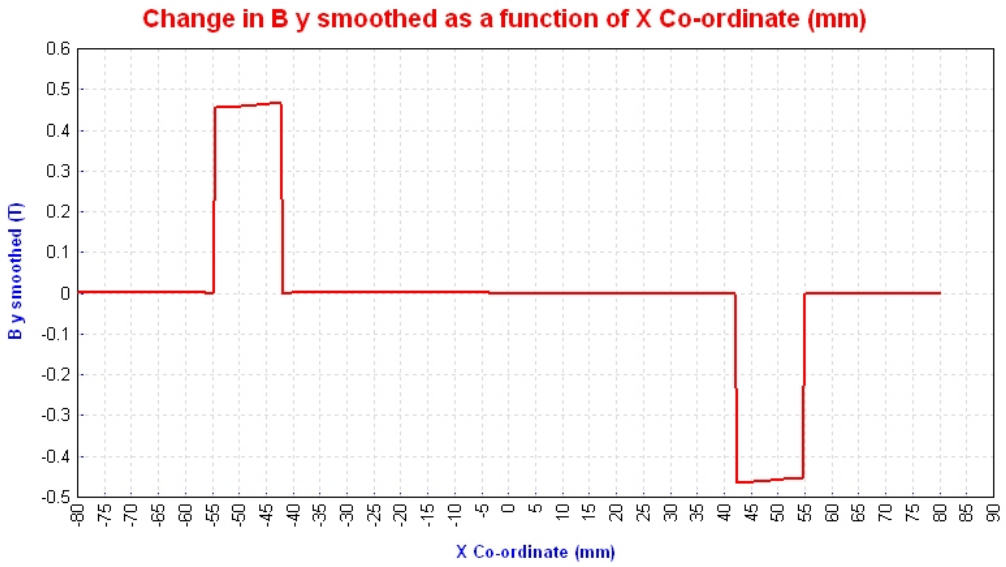

Figure 2-9 Flux Density across the stator core geometry

The magnetic force can be readily obtained from FEA methods. Figure 2-10 shows the magnetic force obtained from the magnetostatic analysis of section 2.1 and the force given by Magnet when the rotor follows a prescribed trajectory and a fixed current is fed through the coils. Figure 2-11 shows a 3-D plot of force values obtained with Magnet. The plot shows the force inverse proportionality with the square of the air gap and its direct proportionality with the square of the current.

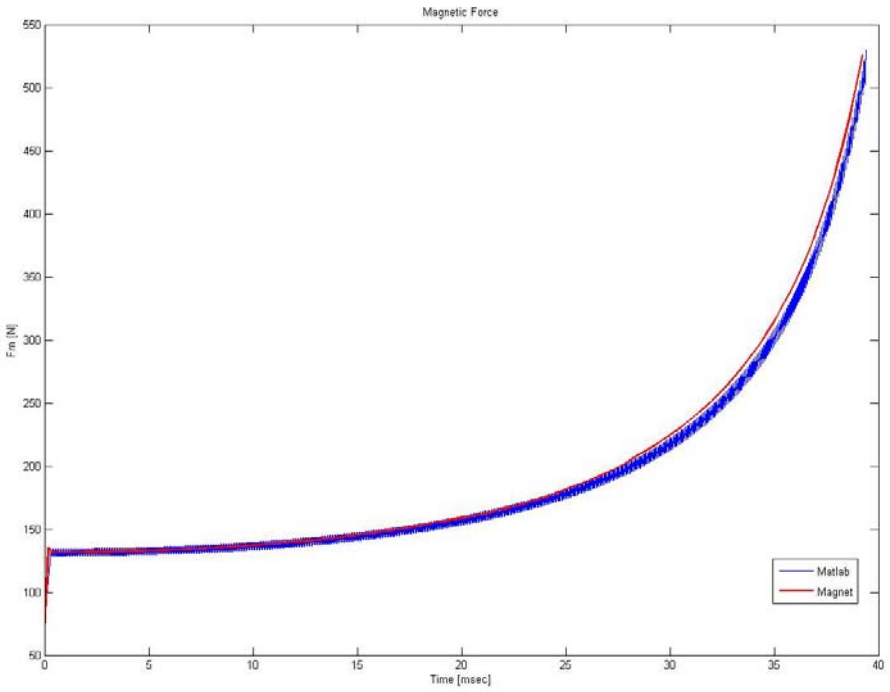

Figure 2-10 Magnetic Force obtained from FEA and Analytical models

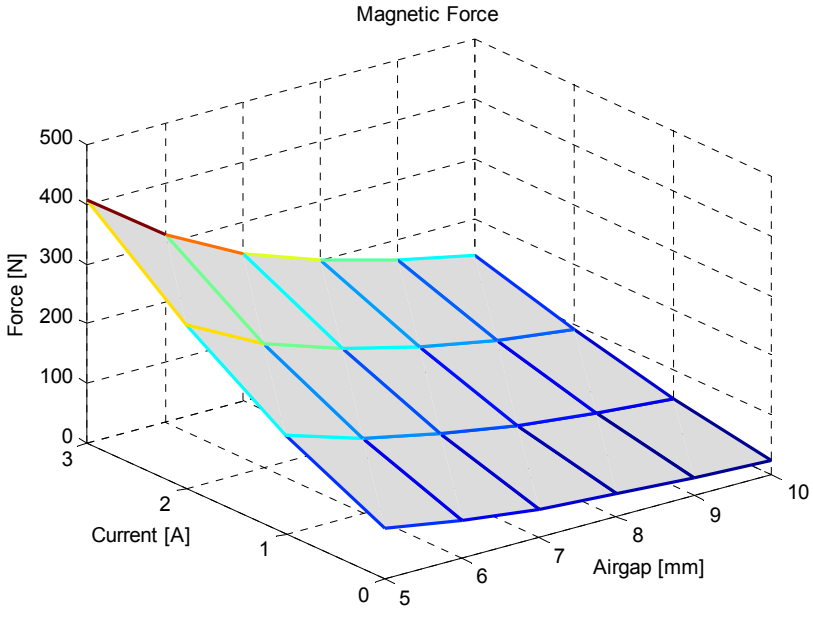

Figure 2-11 Variation of Force with airgap lengths and current

These values of force will be compared to experimental values obtained from measuring the magnetic flux density across the stator face. This comparison will be done for the purpose of model verification in chapter 4 where experimental results will be shown. The Maxwell Stress Tensor method provides a means to obtain the force within the airgap of the maglev. The local normal component of force density can be expressed as [15]

$$f_n = \frac{1}{2\mu_0}\left({B_n}^2 - {B_t}^2\right) \tag{2.13}$$

Where f_n, B_n, B_t denote the normal component of force density in the airgap, normal and tangential component of flux density respectively. The actual forces acting over the stator can be calculated by integrating the force density components over its surface area. If discrete values of the flux density components over a series of uniform surface areas are available the integral can be substituted by a summation over these surface areas. This method can be applied to figure (2-12) where a set of discrete values of normal flux density in the airgap is plotted. The picture shows the flux density in the airgap for a current of 0.65A and an airgap of 5mm which yields a maximum force of 135.3 N.

The proposed position estimation method relies on a model for the system inductance. This static property can also be characterized using FEA methods. In this work the FEA software was used to derive a look-up table for inductance that was later compared to experimental inductance measurements. The simulation consists on the application of a short voltage pulse to the maglev coils. As a result, a linearly varying current was observed and used to determine inductance. The linear variation of current suggests that resistive effects can be disregarded and therefore the inductance can be calculated as

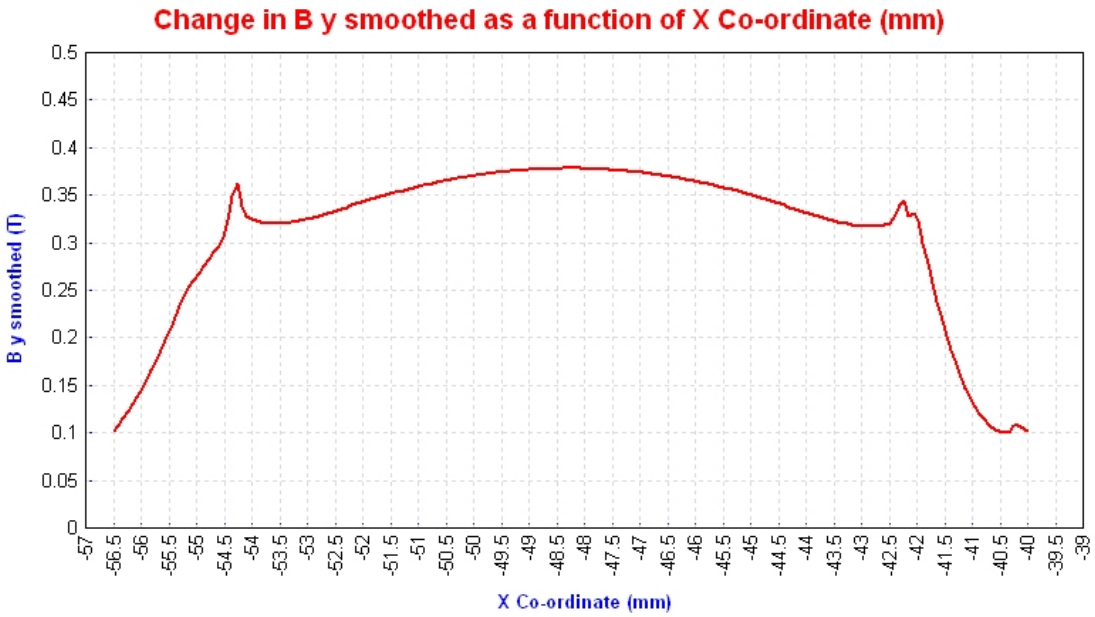

Figure 2-12 Normal Flux density for Ag=5mm and Icoil=0.65A

$$L = V\frac{\Delta t}{\Delta i_c} \tag{2.14}$$

In order to get a linear variation in current, the voltage pulse duration must be

$$T_{pulse} \leq \frac{1}{10}\tau_{RL} = \frac{1}{10}\frac{L_{10mm}}{R_{coil}} \tag{2.15}$$

In other words, the pulse duration must be much less than the maglev R-L equivalent circuit time constant at minimum inductance. A voltage pulse of 100V with a duration of 2 ms was applied during simulation.

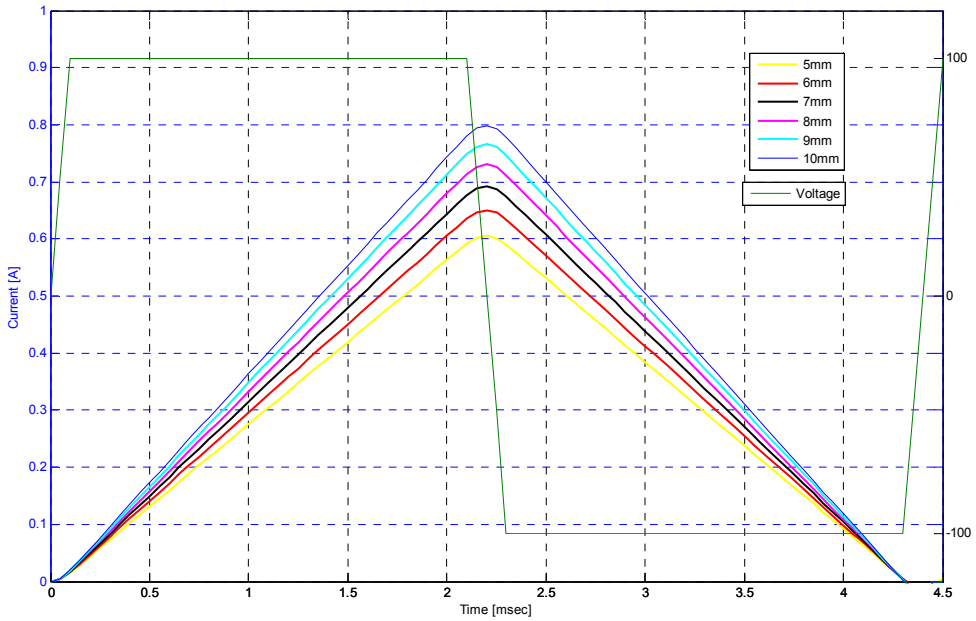

Figure 2-13 Maglev Inductance characterization

Figure 2-13 shows the results obtained with Magnet for 5 - 10mm air gap. Obtaining the λ-I system characteristics offers another way of finding the maglev system inductance. Figure 2-14 shows λ-I plots for different airgap lengths obtained with Magnet software and the derived inductance values are listed in table 2-2. It is seen that the variation in inductance is only 25% of its maximum value. This situation becomes a challenge in position detection since 25% does not represent a large range in the variation of this parameter. In electrical machines, like in the switched reluctance type, this range is much larger and therefore they represent a more suitable scenario for similar position

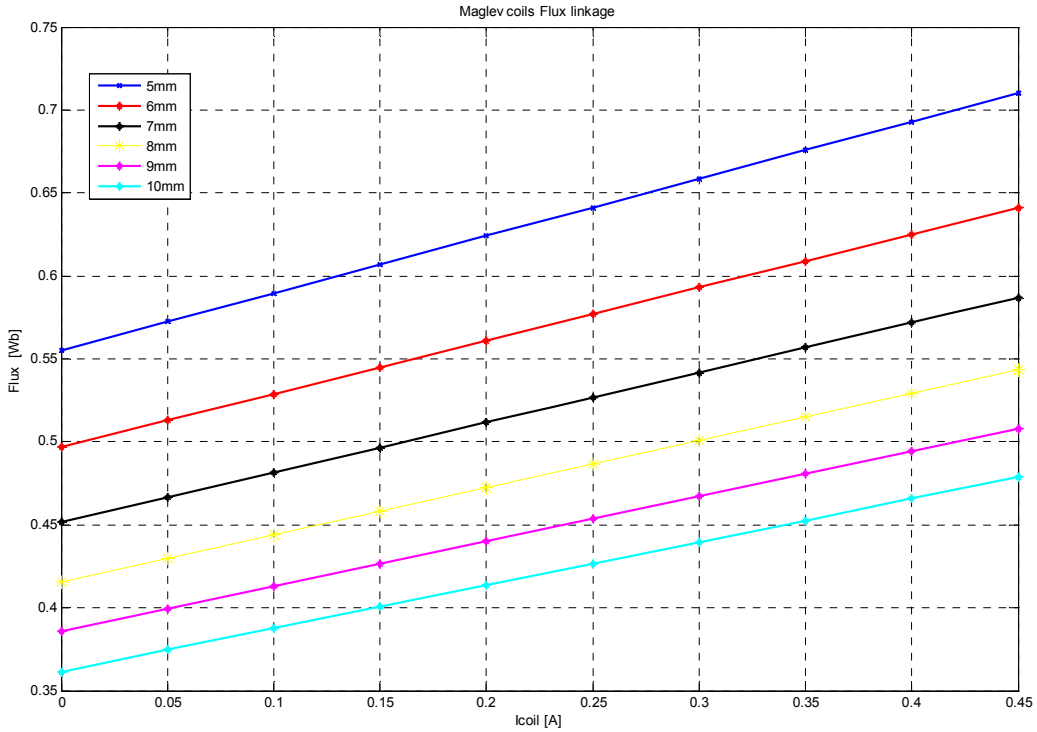

Figure 2-14 λ - I maglev curves

estimation techniques. Table 2-2 also lists the inductance values found when equation (2.14) is used with the plots in figure 2-13. These two results show only a 3% discrepancy and therefore will be used to improve the maglev dynamic model as explained in the next section. Furthermore, these values will be compared with experimental values obtained from the application of Maxwell Stress Tensor method (equation (2.13)) to measurements of magnetic flux density in the airgap.

Table 2-2 Maglev Inductance values

Airgap Length [mm]	Inductance from Equation 2-14 [H]	Inductance from figure 2-14 [H]
5	0.710	0.688
6	0.661	0.640
7	0.621	0.602
8	0.589	0.575
9	0.562	0.546
10	0.539	0.526

2.4 Dynamic Modeling of Maglev System

A free-body diagram of the maglev mechanical system is shown in figure 2-15. The flux in the electromagnets and permanent magnets produces an attracting force F_M between rotor and stator. This force is to overcome the weight of the rotor, which is 45 lbs., to move it upward. The rotor is initially positioned at a distance x of 10mm from the stator. The desired operational air gap between rotor and stator is 5mm. Considering the free-body diagram of figure 2-15 and Newton's 3rd Law of motion, equation (2.16) describes the dynamics of this mechanical system.

$$m\ddot{x} = mg - F_M \tag{2.16}$$

Where m is the levitated object mass, g is the acceleration of gravity, $\ddot{x}$ is the rotor acceleration and F_M is the magnetic force. The magnetic force can be derived from the flux density B in the airgap and was previously found in section 2.1.

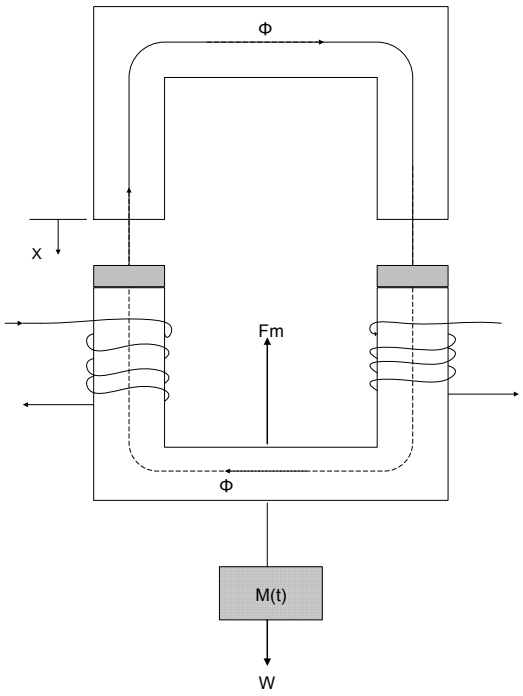

Figure 2-15 Maglev free-body diagram

Application of Kirchoff's Voltage Law and Faraday's Induction Law to the equivalent electrical circuit of Figure 2-16 allows us to derive the following equation for the phase voltage.

$$V = ri + \frac{d\lambda}{dt} \tag{2.17}$$

Where r is coil resistance and λ is the flux linkage in the coil. This flux linkage varies with the coil current and air gap between rotor and stator, therefore $\lambda=\lambda(i,x)$. Also, λ may

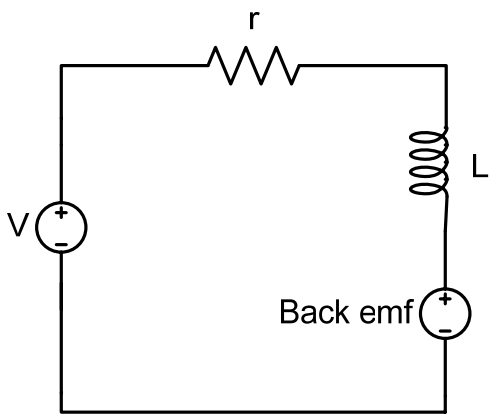

Figure 2-16 Maglev equivalent electric circuit

be regarded as the addition of two components,

$$\lambda = \lambda_i(i, x) + \lambda_m(x) \tag{2.18}$$

Where λ_i is the flux linkage due to the coil current and λ_m is the flux linkage due to the permanent magnets. Replacing equation (2.18) in (2.17) we obtain the following,

$$V = ri + \frac{\partial \lambda_i}{\partial i}\frac{di}{dt} + \frac{\partial \lambda_i}{\partial x}\frac{dx}{dt} + \frac{\partial \lambda_m}{\partial x}\frac{dx}{dt} \tag{2.19}$$

$$V = ri + \frac{\partial \lambda_i}{\partial i}\frac{di}{dt} + \left[\frac{\partial \lambda_i}{\partial x} + \frac{\partial \lambda_m}{\partial x}\right]\frac{dx}{dt} \tag{2.19.a}$$

The term in brackets in equation (2.19.a) is the Back emf in figure 2-16 and $L = \partial\lambda_i/\partial t$ is the system's inductance. It is necessary to find an expression for the flux linkage to determine an equation that describes the dynamics of this electromagnetic system. A characterization of permanent magnets (PM) is crucial for the derivation of an equivalent magnetic circuit. This magnetic equivalent circuit and the derivation of an expression for the flux linkage in the air gap were covered in section 2.1. The combination of equations (2.8) and (2.9) yields the following expression for the flux linkage in the coils

$$\lambda = 2N\mu_0 A_g \left[\frac{Ni + H_c L_m}{x + \mu_0 A_g R_m}\right] \tag{2.20}$$

Where A_g is the airgap cross-sectional area and $R_m=L_m/(\mu_{rm}\mu_0 A_m)$ is the permanent magnet reluctance. The one parameter that needs special attention in equation (2.20) is A_g. In this particular application the effective airgap cross-sectional area is a function of the airgap length x and the coil curren i. This parameter was first assumed to be equal to A_m, the magnets cross-sectional area, but the values of flux linkages and their corresponding values of inductance were far from those obtained from measurements and FEA analysis. In order to obtain a reliable dynamic model with equation (2.20), the results from FEA analysis were used to fine tune the parameter A_g. Figure 2.17 shows a plot of A_g as a function of current and airgap length. These are the values used in the dynamic model of the maglev that provided a good match with experimental results.

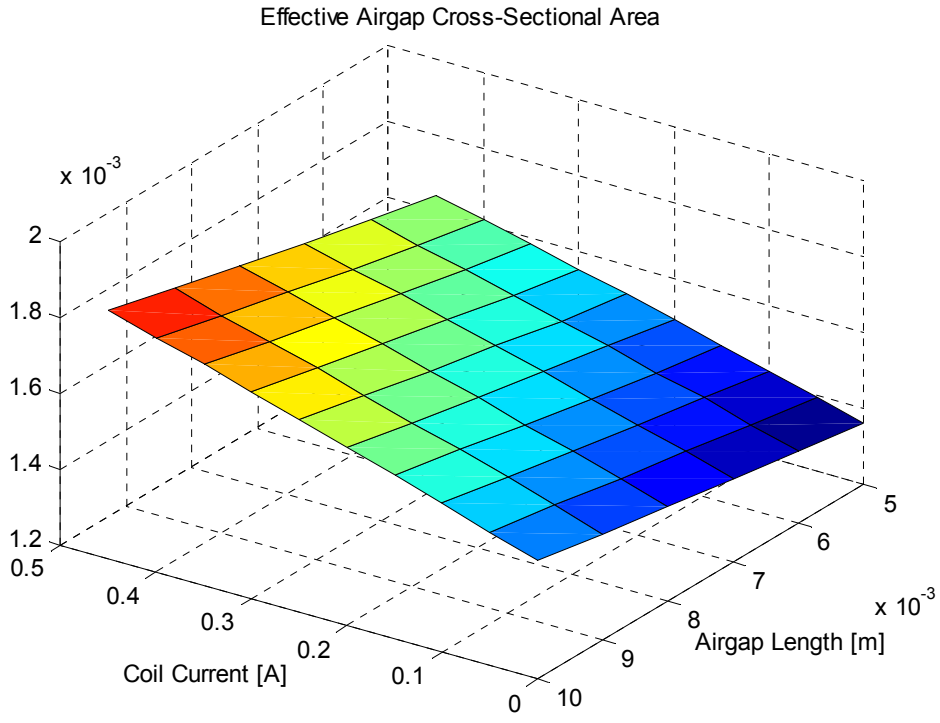

Figure 2-17 Effective Airgap cross-sectional area

The combination of equations (2.8), (2.19.a) and (2.20) finally yields the expression used for dynamic modeling of the electromagnetic system:

$$V = ri + \frac{K_2}{x + \mu_0 A_{Ag} R_m}\frac{di}{dt} - \left[\frac{K_2 i + K_3}{\left(x + \mu_0 A_{Ag} R_m\right)^2}\right]\frac{dx}{dt} \qquad (2.21)$$

Where $K_2 = 2N^2\mu_0 A$, $K_3 = 2N\mu_0 A K_1$. A Maglev Simulink® model has been implemented using equations (2.12.a), (2.16) and (2.21) to study the proposed sensorless control .

Figure (2-18) shows the maglev Simulink® model where the following building blocks can be identified: Maglev, Hysteresis Current control, Mode control, Acceleration, Regulation, and Air gap Estimator.

The Maglev block contains the equations representing the dynamic of this electromechanical system. It is the implementation of equations (2.12.a), (2.16.) and (2.21). The Hysteresis Current control block simulates the Semikron full-bride converter and its controlling logic. This block applies the correct DC voltage to the coils depending on the coil current value and maintains this value within a specified current hysteresis band of I_{ref} ± 5%. The Mode control decides who sets the reference current for the Hysteresis current control block. This reference current can be provided by either the acceleration block or the regulation block. The Acceleration block acts during system start-up and it is in charge of bringing the levitated element (rotor) within the position hysteresis band. This block contains a current look-up table that was initially determined with FEA analysis and fine-tuned during testing. These values of currents will produce a small upward acceleration of the rotor until the regulation block takes control over the reference current signal generation. The regulation block is another implementation of hysteresis control, but this time the controlled signal is the rotor position. The position hysteresis band used in this simulation was also x_{ref} ± 5%.

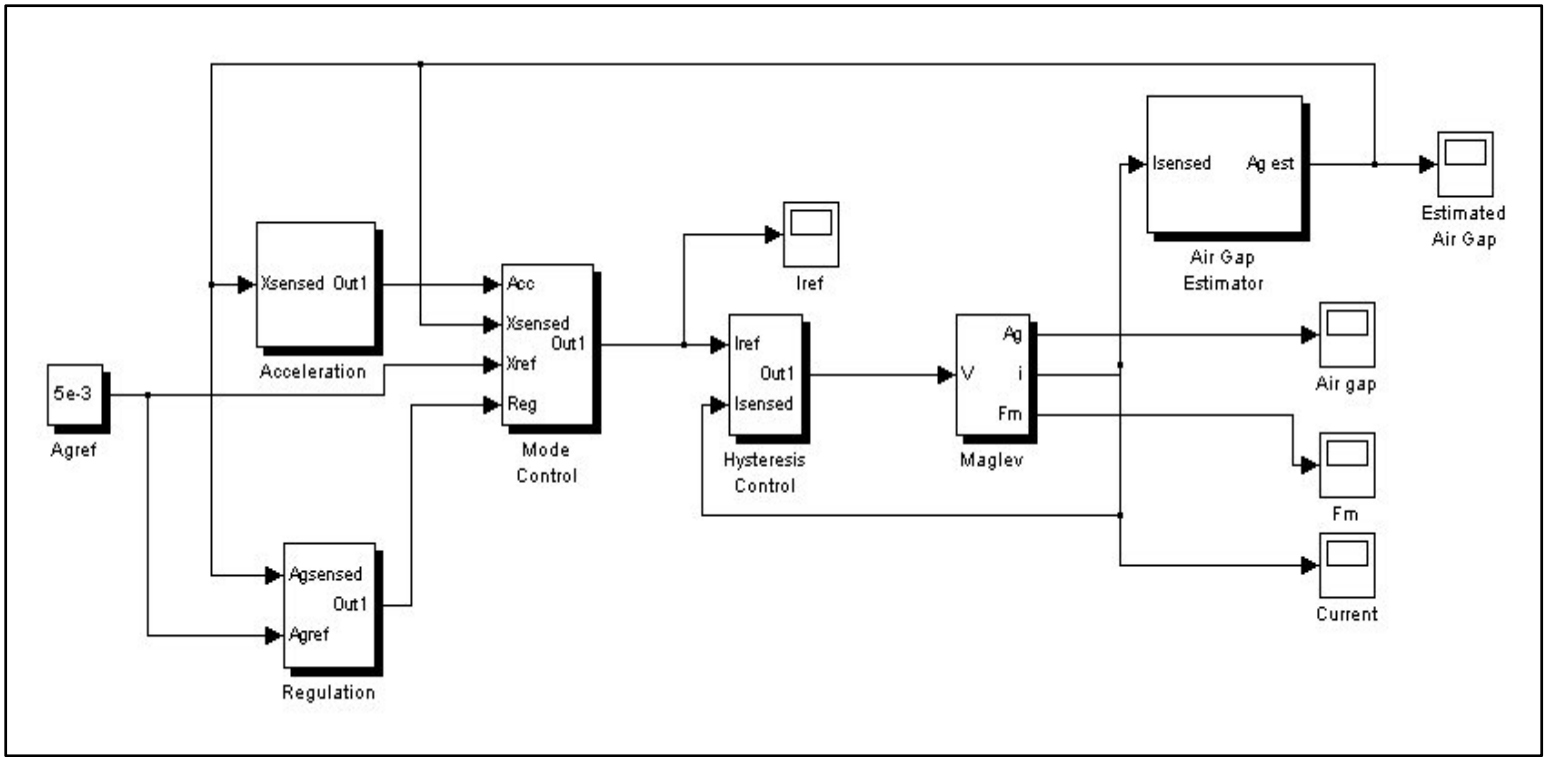

Figure 2-18 The maglev Simulink model

2.5 Stability considerations in closed loop control of Maglev systems

The static force of attraction used in EML systems presents an inverse force-distance characteristic, as shown in figure 2-11. This characteristic, known as negative stiffness, make the maglev system inherently unstable. Therefore a control system is necessary to obtain a stable operation. The function of the control action would be to modify the force-distance characteristics of the system providing a positive stiffness, i.e. for an increase in airgap length the attracting force must increase and vice versa.

The fundamental requirement in electromagnetic levitation suspension (attraction type) systems is its capability of sustaining stable equilibrium under all operating conditions and disturbances. In addition to payload variations, maglev systems in transportation applications are subject to three sources of excitation, namely, unsteady aerodynamic forces, guideway induced vibrations and continuous vibrations owing to guideway roughness and misalignments [16].

A control system must provide adequate suspension stiffness for "track holding" properties, and sufficient damping to control resonant response, but soft enough to follow the low-frequency profile of the guideway beams [16].

Suspension stiffness is the ratio of change in airgap length to change in paylod weight, and is related to the steady-state error in the position control loop. Guideway oscillations can bring a resonance condition caused by the dynamic interaction between guideway vibration and suspension control systems. Therefore, adequate separation between the guideway natural frequency and suspension needs to be introduced. The damping characteristic of the suspension system must allow good ride quality. Ride

quality specifications are often given in terms of the maximum permissible vertical acceleration levels that are closely related to the overall damping of the system.

The proposed position closed-loop controller effectively provides positive stiffness to the maglev by modifying its force-distance characteristics. It is seen in figure 2-20 that the force increases as the increase in payload tends to increase the airgap length.

The magnetic force in equation (2.12.a) can be written as

$$F_M = \mu_0 A_{Ag} \left[\frac{Ni + K_1}{x + \mu_0 A_{Ag} R_m} \right]^2 = K \left[\frac{I}{X} \right]^2 \tag{2.22}$$

Where $K=\mu_0 A_{Ag}$, $I=Ni+K_1$ and $X=\mu_0 A_{Ag} R_m$. Linearization of this function around an operating point yields,

$$F_M^* = K \frac{I_0}{X_0^2} I^* - K \frac{I_0^2}{X_0^3} X^* = K_I I^* - K_X X^* \tag{2.16}$$

Where $K_I = K \cdot (I_0/X_0^2)$, $K_X = K \cdot (I_0^2/X_0^2)$, $I^* = i - I_0$ and $X^* = x - X_0$. Equation (2.16) can then be rewritten as

$$m\ddot{X}^* = K_X X^* - K_I I^* + mg \tag{2.17}$$

The state variables $Z_1 = X^* - \alpha$ and $Z_2 = \dot{X}^*$, where α is any desired final position, are chosen to arrange equation (2.17) in state space format. This selection of state variables yields,

$$\begin{cases} \dot{Z}_1 = Z_2 \\ \dot{Z}_2 = \dfrac{K_X}{m} Z_1 - \dfrac{K_I}{m} u + g \end{cases} \tag{2.18}$$

The input u is chosen to be

$$\begin{cases} u = \dfrac{M}{2} sign(s) + \dfrac{M}{2} + i_{min} \\ s = Z_1 - \alpha \end{cases} \tag{2.19}$$

Where *s* is the switching surface and $0<M<.i_{max}$. To establish stability of system (2.18), the candidate Lyapunov's function is chosen as

$$V(Z) = C_1 Z_1^2 + C_2 Z_2^2 \qquad C_1 > 0, C_2 > 0 \tag{2.20}$$

$$\dot{V} = 2C_1 Z_1 Z_2 + 2C_2 Z_2 \left[\frac{K_X}{m} Z_1 - \frac{K_I}{m} u(Z) + g\right] \tag{2.21}$$

When the state hit the switching curve equation (2.21) becomes

$$\dot{V}(Z) = Z_2 \left[2C_1 \alpha + 2C_2 \frac{K_X}{m} \alpha - 2C_2 \frac{K_I}{m} (M + i_{min}) + 2C_2 g\right] \tag{2.22}$$

Since $Z_2<0$ the term in brackets must be always positive to have a negative semi-definite $\dot{V}$ function. Equation (2.22) provides a means to determine the parameter α as follows,

$$\alpha > \frac{C_2 \frac{K_I}{m} (M + i_{\min}) - C_2 g}{C_1 + C_2 \frac{K_X}{m}} \tag{2.23}$$

Equation (2.23) determines a lower bound for the position hysteresis band given the upper and lower limits in coil current. Lyapunov's theorem for stability establishes that the selection of α according to (2.23) guaranties the system local stability.

Equation (2.23) could also be used to determine the maximum coil current that will ensure stability. Once a hysteresis band has been chosen this maximum current value could be determined by solving (2.23) for *M*.

2.6 Discussion of simulation results

This section shows the results obtained with the dynamic model of section 2.4. The most important characteristics to consider for model verification are inductance, force and flux linkage. Simulation results from the maglev closed-loop operation are also presented to illustrate the usefulness and merits of the dynamic model. All simulation parameters of this simulation are listed in table 2-3.

Table 2-3 Maglev closed-loop operation simulation parameters

Simulation Parameter	Symbol	Value	Units
Number of Coil turns	N	600	
DC Bus Voltage	V	300	[V]
Coil Resistance	r	9.11	[Ohm]
Magnet Coercivity	H_c	8.38×10^5	[A/m]
Magnet Retentivity	B_r	1.1	[T]
Rotor Stack Length	L	0.1016	[m]
Air gap width	a	0.0127	[m]
Rotor weight	W	170-300	[N]
Gravitational constant	g	9.81	[m/s^2]
Rotor Initial Position	x_0	0.01	[m]

The expression for flux density in the magnets B_m given by equation (2.8) suggests that the challenge in obtaining a good dynamical model is in the choice for the airgap cross-sectional area A_{Ag}. This area varies with respect to the coil current i and the

airgap length x. Figure 2-17 shows the mapping provided by FEA methods for A_{Ag} in the region of interest. The validity of results from FEA analysis was first verified with experimental measurements. FEA was used to tune the dynamic model only after seeing the good match between these two results (FEA and experimental). Figure 2-10 shows the closeness in force calculation between FEA analysis and the analytical model. The most important static characteristic is the inductance of the maglev due to its one-to-one correspondence with the airgap length. Table 2-4 lists the values of inductances computed from the λ-i maglev characteristics calculated with the analytical model.

Table 2-4 Maglev inductance values from analytical model

Airgap [mm]	Inductance [H]
5	0.681
6	0.633
7	0.598
8	0.570
9	0.541
10	0.522

The above listed inductance values were computed from the λ-i plots of figure 2-19. The plots are very similar to those shown for FEA analysis which rendered good matching results between numerical and experimental results

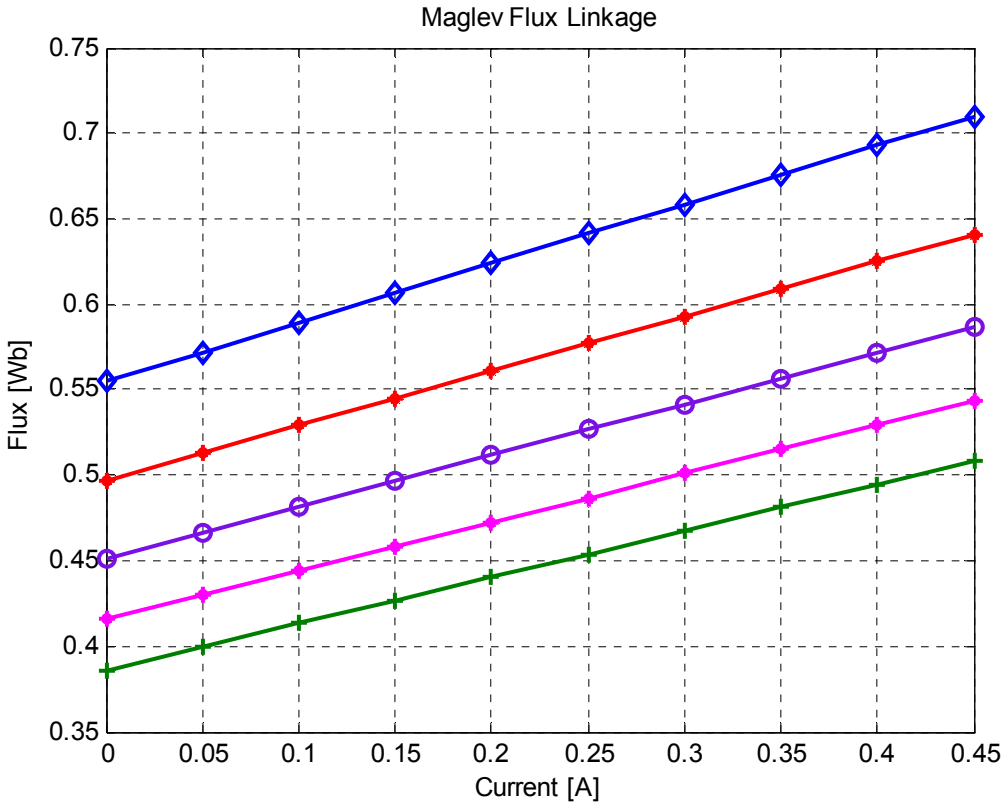

Figure 2-19 λ-i maglev characteristics from analytical modeling

The maglev closed-loop operation simulation starts with the rotor at x_0 = 10mm. After the rotor settles in the desired position hysteresis band, the payload is varied in two different steps of 10% and 20% of the initial weight. Figure 2-20 shows the rotor position evolution during simulation. The figure shows the effectiveness of the position controller in maintaining the rotor within the desired band of 5mm±5% regardless of changes in payload.

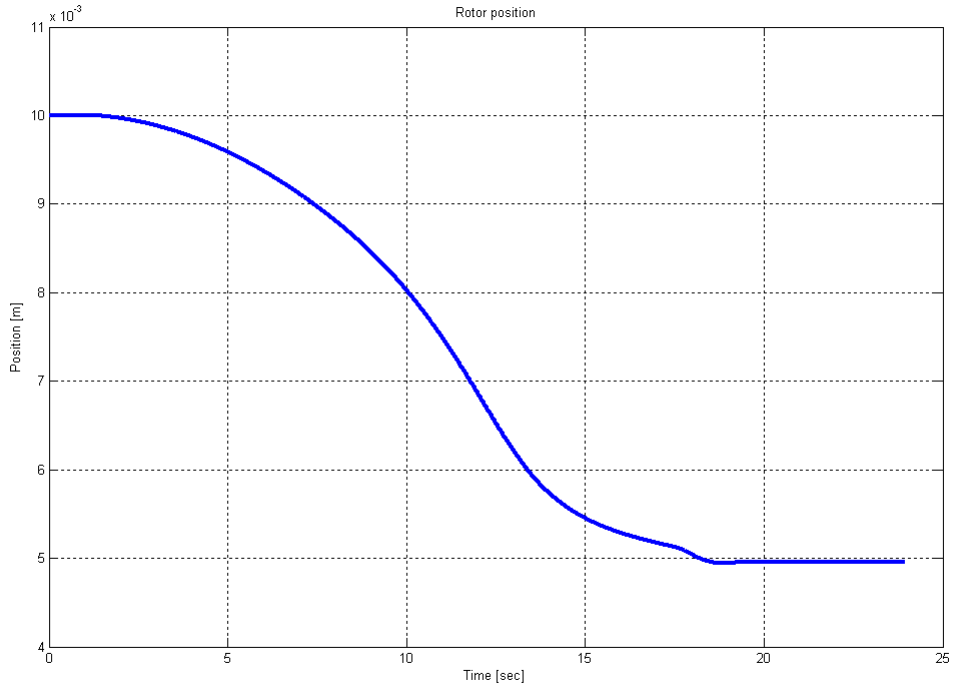

Figure 2-20 Rotor position evolution

The magnetic force in this simulation is shown in figure 2-21. There are two distinctive characteristics in this plot. The force is approximately constant in the transition area from initial position until the rotor enters the hysteresis position band.

Once the rotor enters this hysteresis band, the magnetic force is created by the reference current set by the position hysteresis controller. The force shows high frequency variations around the values that compensate the rotor weight, effectively levitating the rotor in the hysteresis band. This variation in force is filtered by the rotor dynamics which is a result of the fundamental assumption of this estimation method, namely, the system's mechanical time constant is much larger than the electrical time constant.

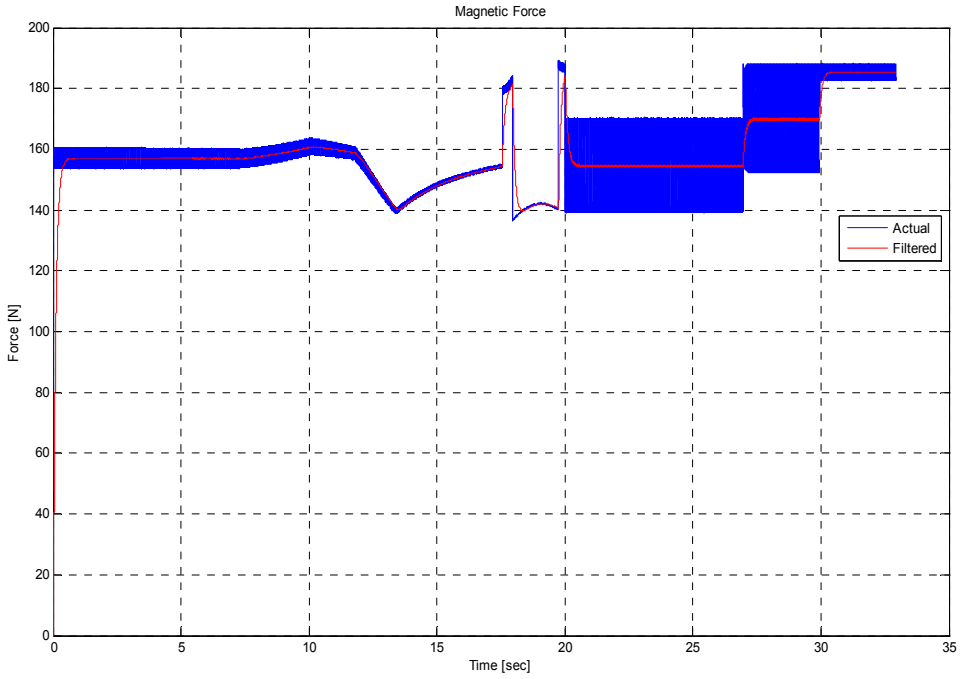

Figure 2-21 Magnetic force

The coil current is shown in figure 2-22. This simulation result played a very important role in actual hardware selection and implementation. First of all, it provided a good starting point for determination of parameters like hysteresis current and position bands, acceleration block look-up table, full-bridge maximum switching frequency, and maximum and minimum current values for hysteresis current control. Figure 2-22 shows that the current has a good reference tracking performance. In the hysteresis band this figure shows how the current oscillates around the current value that compensates for gravity effects allowing the levitation of the rotor. This value is:

$$i_e = \sqrt{\frac{mg}{A\mu_0 N^2}\left[x_e + \frac{H_c L_m \mu_0}{B_r}\right]} - \frac{H_c L_m}{N} \qquad (2.22)$$

The coil current and its filtered values are shown in figure 2-22 where it is clear the oscillation of the current around the values determined by (2.22). Another important characteristic to notice is that the current oscillations in the hysteresis band increase in frequency as the rotor payload is increased. This behavior occurs as a result of faster rotor dynamics. Equation (2.16) determines that the rotor acceleration in the direction of gravity will increase and the acceleration produce by the magnetic force will decrease with the rotor payload mass. In other words, when the minimum current is applied to the coils the rotor will drop faster and therefore it is necessary to switch to maximum current more often.

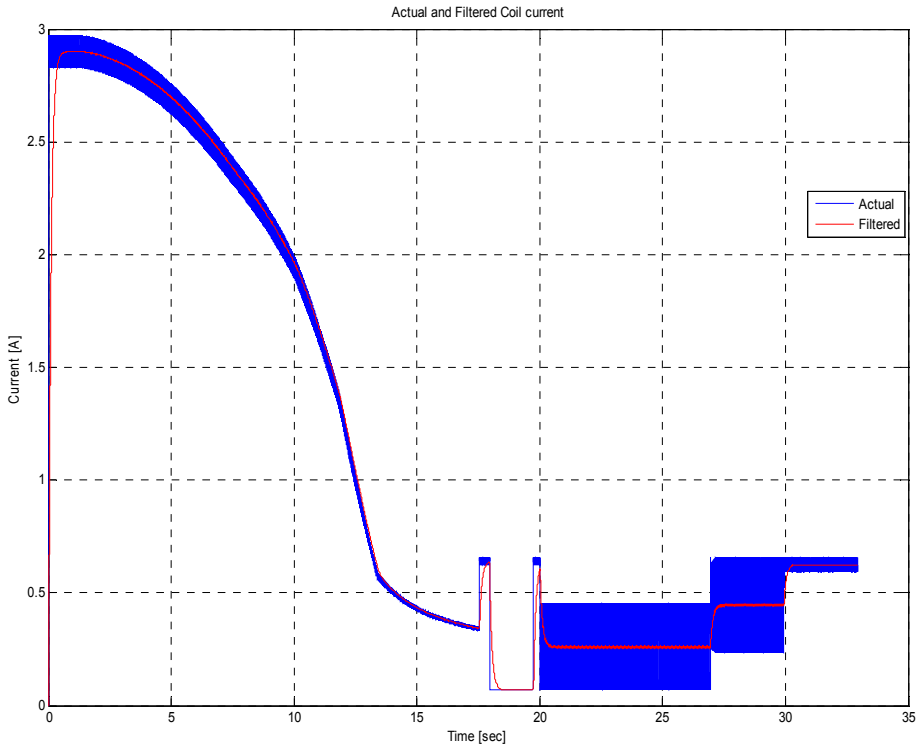

Figure 2-22 Maglev coil current

Another important observation is that the swings of coil current decrease with weight. This is a result of coil inductance. The coil current time variation (*di/dt*) is limited by the DC bus voltage and coil inductance. Since neither of them is changing and the reference current changes faster, the current has less time to swing between the upper and lower limits in the hysteresis band. This result provided important insight in the selection of the power electronic converter. It was observed that the maximum switching frequency was 3.5 KHz.

CHAPTER 3

ELIMINATION OF POSITION SENSORS IN MAGLEV

This chapter explains the theoretical issues of the proposed sensorless position estimation. It also looks at some implementation and geometrical considerations that influence the effectiveness of the method. In addition, some simulation results are shown to provide a sense of its usefulness and value in predicting real implementation issues.

3.1 Active phase sensorless technique

In terms of technology, the proposed sensorless position estimation can be regarded as speed intensive or MIPS (millions of instructions per second) intensive. It relies on the computational power of modern microcontrollers and the fact that mechanical time constants are much larger than electrical time constants. In speed intensive techniques differential equations governing the dynamics of the electromechanical device along with analytical expressions for magnetic characteristics are solved to extract position information [17].

In the case of the maglev system, measurements at the electromagnet coils terminals (active phase) are taken for on-line calculation of the system's inductance. This magnetic signature possesses a one-to one correspondence with the levitated object's position. The inductance-to-position mapping of table 2-2 is store in memory in the form of a table lookup.

The voltage equation (2.19) of the active phase provides a means for on-line calculation of inductance. Looking at the current waveform of figure 3-1, the voltage equation can be evaluated at two instances of time -ξ before a transition and +ξ after a transition. Equation (2.19) becomes

$$V^{+} = ri + L(x)\left(\frac{di}{dt}\right)^{+} + \left[\frac{\partial \lambda_i}{\partial x} + \frac{\partial \lambda_m}{\partial x}\right]\left(\frac{dx}{dt}\right)^{+} \tag{3.1}$$

$$V^{-} = ri + L(x)\left(\frac{di}{dt}\right)^{-} + \left[\frac{\partial \lambda_i}{\partial x} + \frac{\partial \lambda_m}{\partial x}\right]\left(\frac{dx}{dt}\right)^{-} \tag{3.2}$$

Subtraction of (2.2) from (2.1) yields

$$V^{+} - V^{-} = L(x)\left[\left(\frac{di}{dt}\right)^{+} - \left(\frac{di}{dt}\right)^{-}\right] + \left[\frac{\partial \lambda_i}{\partial x} + \frac{\partial \lambda_m}{\partial x}\right]\left[\left(\frac{dx}{dt}\right)^{+} - \left(\frac{dx}{dt}\right)^{-}\right] \tag{3.3}$$

Considering that the rotor speed does not change significantly at these two instances, the difference in rotor speed is negligible and therefore the second term in equation (3.3) vanishes. This situation is not unrealistic if the difference in mechanical and electrical time constants is considered or if the rotor is at standstill.

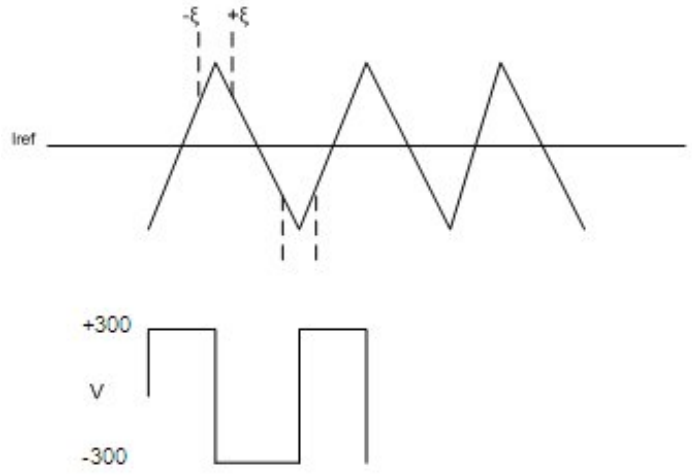

Figure 3-1 Active phase current and voltage

Equation (3.3) translates into equations (3.4) and (3.5) which are the backbone of the proposed sensorless method.

$$600 = L(x)\left[\left(\frac{\Delta i}{\Delta t}\right)^{+} - \left(\frac{\Delta i}{\Delta t}\right)^{-}\right] \tag{3.4}$$

For a negative-to-positive transition in coil current and

$$-600 = L(x)\left[\left(\frac{\Delta i}{\Delta t}\right)^{+} - \left(\frac{\Delta i}{\Delta t}\right)^{-}\right] \tag{3.5}$$

For a positive-to-negative transition in coil current. By on-line measurement of the phase current and voltage, the maglev inductance can be calculated according to (3.4) and (3.5). Figure 3-2 shows the flow diagram of the sensorless method.

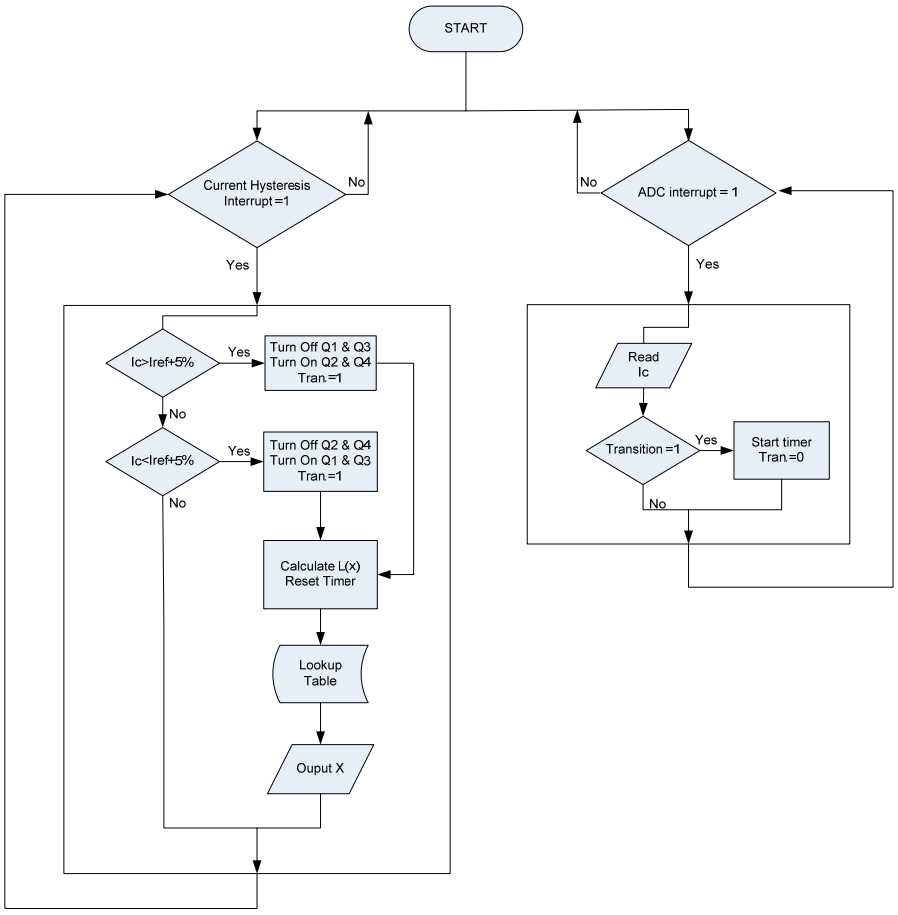

Figure 3-2 Sensorless estimation algorithm flow chart

This routine was implemented on a TMS320F2812 DSP microcontroller. The diagram shows the two main interrupts where current sampling and hysteresis current control occur.

3.2 Sensitivity analysis with respect to geometrical quantities

The sensorless method relies on a geometry- dependent static quantity like inductance. In section 2.1 a magnetic equivalent circuit analysis was performed to determined the flux linkage that eventually allowed us to make a mapping between rotor position and inductance. That expression certainly shows a dependency on geometry of the magnetic circuit since reluctances of that circuit determine the flux and therefore the flux linkage. This section looks at variations in the geometry of the magnetic circuit that effectively change the reluctances found in the trajectory followed by the magnetic flux. A vertical and horizontal displacement of the rotor will increase the airgap and its reluctance. A vertical displacement is considered normal operation and all equations and models were developed under this assumption. On the other hand, a misalignment caused by a horizontal displacement of the rotor will change the reluctances in a way that was not accounted for during modelling.

One parameter to consider for exploration of the effects of geometrical changes on the sensorless method is the flux linkage since this quantity is closely related to system inductance. By considering the change in flux linkage an therefore the change in inductance , the sensitivity of the system can be studied using equations (3.4) and (3.5). Figure 3-3 shows the rotor and stator configuration at a maximum misalignment of 6mm with respect to their center. This situation really represents an extreme condition since in

most practical maglev transportation applications the desired airgap for suspension and guidance is 10mm.

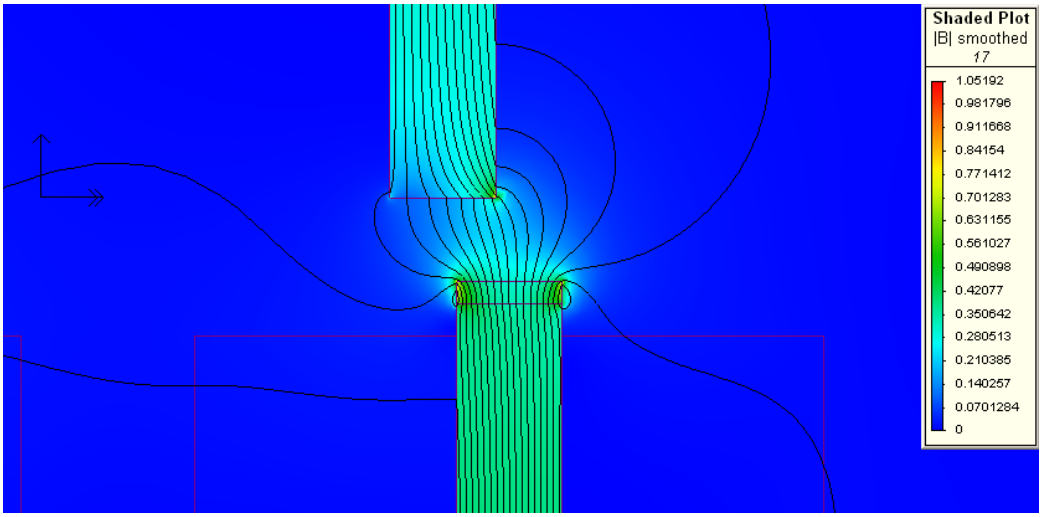

Figure 3-3 Rotor-stator misalignment

As seen in figure 3-3, this misalignment deteriorates the flux behavior by increasing leakages and fringing effects. Intuitively, one can expect the inductance to decrease under these circumstances which will be interpreted as an increase in vertical position on the rotor. However, from figure 3-4 it is seen that the variation in flux linkage λ when the rotor is moved horizontally from its aligned position is not significant. The largest variation (approximately 8%) occurs when the rotor is at 5mm. This is due to the fact that at smaller airgaps the flux leakage decreases and a variation in the average length of any reluctance in the circuit will have a greater impact on the resultant flux. On the other hand, larger airgaps cause more flux leakage and therefore the flux linkage is less sensitive to variation s in reluctance. This decrease in sensitivity makes the estimation of larger airgaps more difficult since the incremental change in inductance per increment in airgap is reduced.

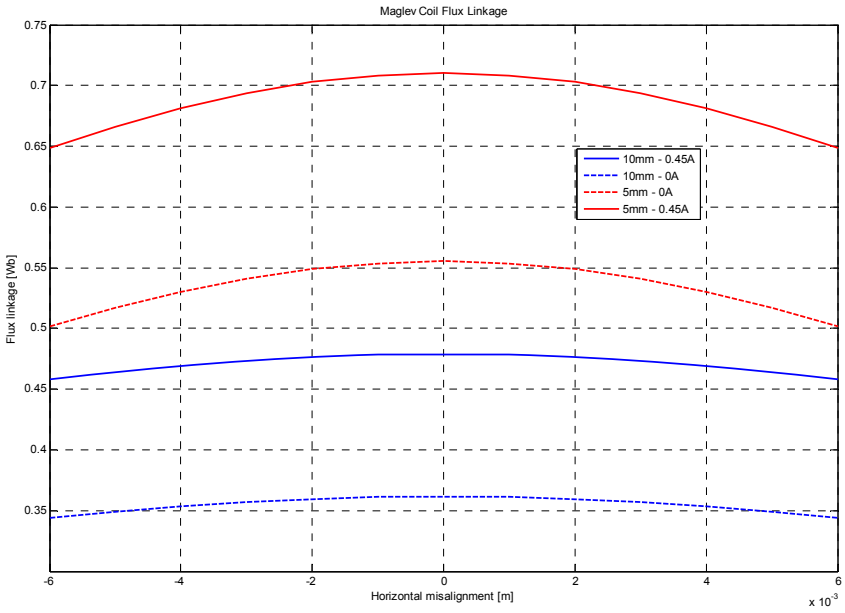

Figure 3-4 Flux linkage variation due to rotor-stator misalignment

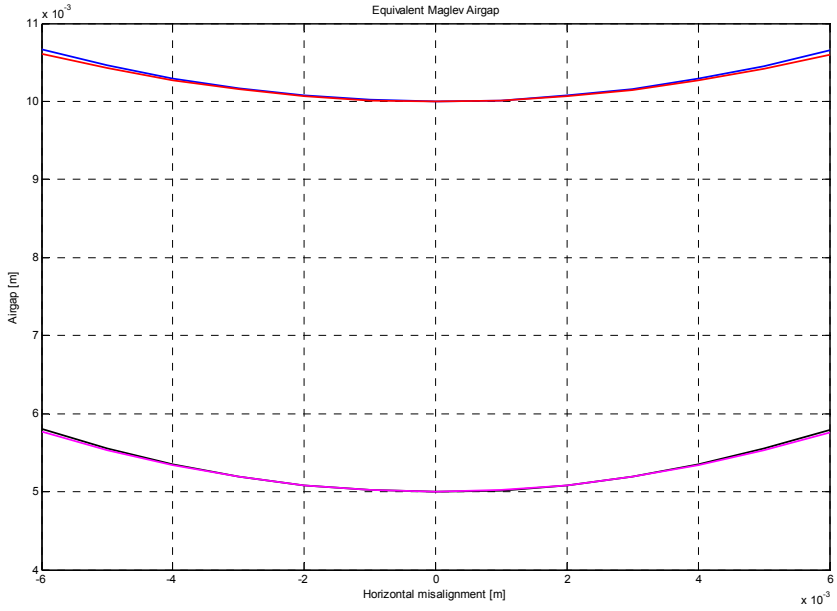

Figure 3-5 Variation in airgap length due to rotor-stator misalignment

Figure 3-5 presents the variation in estimated airgap due to rotor-stator misalignment. The sensitivity to this change in geometry is more noticeable at smaller airgaps where a

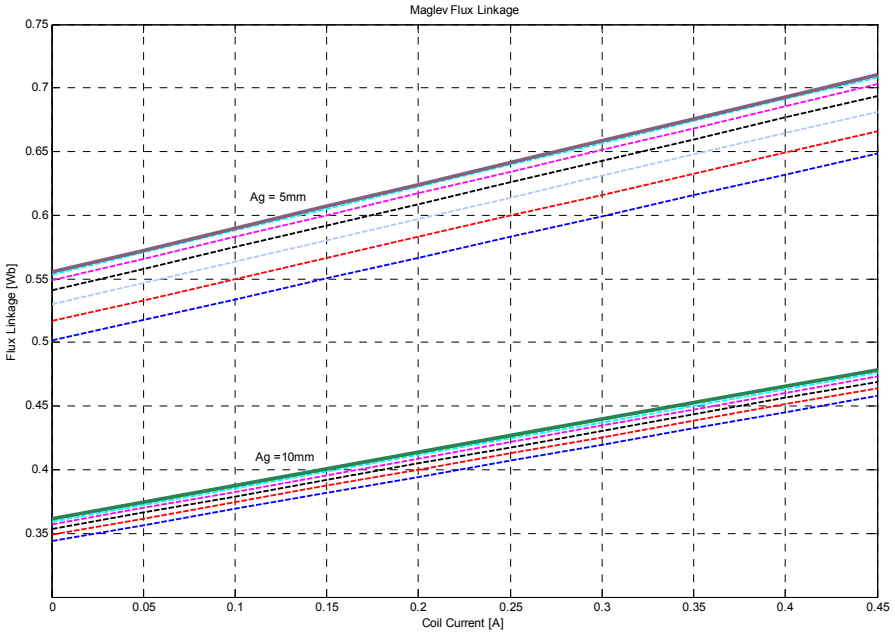

Figure 3-6 Variation in λ-i characteristics due to stator-rotor misalignment

Table 3-1 Estimated Airgap length variation due to rotor-stator misalignment

Horizontal misalignment [mm]	Airgap = 5mm			Airgap = 10mm		
	Icoil = 0 A	Icoil = 0.45A	%	Icoil = 0 A	Icoil = 0.45 A	%
6	0.00580	0.00576	15.4	0.0107	0.0106	7
5	0.00555	0.00553	10.8	0.0105	0.0104	5
4	0.00535	0.00534	7	0.0103	0.0103	3
3	0.00520	0.00519	4	0.0102	0.0102	2

Table 3-1 Continued

2	0.00508	0.00508	1.8	0.0101	0.0101	1
1	0.00502	0.00502	0.6	0.010	0.010	0
0	0.00499	0.00499	0	0.010	0.010	0

change of up to 15.4% is observerd. Table 3-1 summarizes the changes in estimated airgap for different airgap lengths under rotor-stator misalignment.

The previous results can be inferred by considering the sensitivity of the flux linkage in the coil with respect to the airgap reluctance. Since a rotor-stator misalignment will change the effective airgap reluctance, this figure quantifies how bad or good the sensorless method performs in the presence on geometric variations.

Sensitivity is this case is defined as the proportional change in flux linkage to a proportional change in airgap reluctance and may be computed as

$$S_{R_g}^{\lambda} = \frac{\partial\lambda/\lambda}{\partial R_g/R_g} \tag{3.6}$$

The flux linkage given by equation (2.20) can be rewritten as

$$\lambda = 2N\frac{A_m}{A_g}\left(\frac{Ni + H_c L_m}{R_g + R_m}\right) \tag{3.7}$$

$$S_{R_g}^{\lambda} = \frac{\partial\lambda}{\partial R_g}\frac{R_g}{\lambda} = \frac{R_g}{R_g + R_m} < 1 \tag{3.8}$$

Equation (3.8) confirms the observations made from figures 3-4 to 3-6. For an increase in airgap reluctance the flux linkage decreases and the proporcional change in flux linkage is larger for smaller airgaps.

3.3 Sensitivity analysis with respect to current sensor resolution

Current resolution is another important parameter that has a direct effect on the position estimation. Not only this parameter is important for current control purposes, but since the online inductance calculation relies on the time variation of coil current the current sensor becomes a central component in successful implementation of this estimation method. Equations (3.4) and (3.5) provide a means to find an expression of inductance in terms of current sensor resolution.

The resolution of a sensor is defined as the smallest detectable incremental change of input parameter (in this case current) that can be detected in the sensor's output signal. The calculation of inductance requires on-line computation of current change Δi in a defined time interval Δt. The smallest change in inductance will be detected when the next change in current (Δi^{+}) equals the sensor's resolution, therefore that value of inductance can be written as

$$L(x) = \frac{V^{+} - V^{-}}{\frac{\Delta i^{+}}{\Delta t} - \frac{\Delta i^{-}}{\Delta t}} = \frac{600}{\frac{P}{\Delta t} - \frac{\Delta i^{-}}{\Delta t}} \tag{3.9}$$

for a negative-to- positive coil current transition and P is the current sensor resolution. The sensitivity of the inductance with respect to sensor resolution can be evaluated from (3.9) as

$$S_P^L = \frac{\partial L}{\partial P}\frac{P}{L} = -\frac{P}{P - \Delta i^{-}} = \frac{P}{P + \Delta i^{-}} < 1 \tag{3.10}$$

since $\Delta i^{-} < 0$ for a negative-to-positive transition, the sensitivity is always less than minus one. Equation (3.10) suggests that for a smaller sensor resolution (better resolution) the proportional detectable change in inductance will be larger than a sensor with larger resolutions (worse resolution).

3.4 Simulation Results

The results presented in this section correspond to the simulation of the dynamical model developed and explained in section 2.4, but with the rotor position estimator added to the model. All simulation parameters are listed in table2.3.

The results illustrate that the proposed method is feasible and effective, and therefore provided a good starting point for further development and research. The 4^{th} order fixed-step Runge-Kutta integration method was used for the nonlinear differential equations that describe the maglev

The simulated measured and estimated air gaps (rotor positions) are shown in figure 3-7. It is observed that estimated air gap values are very close to actual rotor position. Furthermore, the controller is able to regulate the rotor position within the desired hysteresis band of $x_{ref} \pm 5\%$ regardless of the change in payload weight shown in figure 3-8. A special note on the simulation time step should be made. This is a very critical parameter in the simulation, since a bad choice in the time step can lead to oscillations. It was seen that a time step of 10^{-4} or less should be used to get consistent results.

The estimation error, shown in figure 3-9, exhibits a better match between actual and estimated position values in the regulation band. This is because the increments in system inductance are larger as the rotor approaches the stator and therefore the estimation is more accurate. This fact was also inferred from the geometrical sensitivity analysis of the previous section and is confirmed by experimental results. The Simulink® model does not include measurement noise and therefore it is expected that the actual estimation error will be of larger magnitudes. However, in the actual

implementation the noise was filtered out using signal processing techniques which allowed the method render good results.

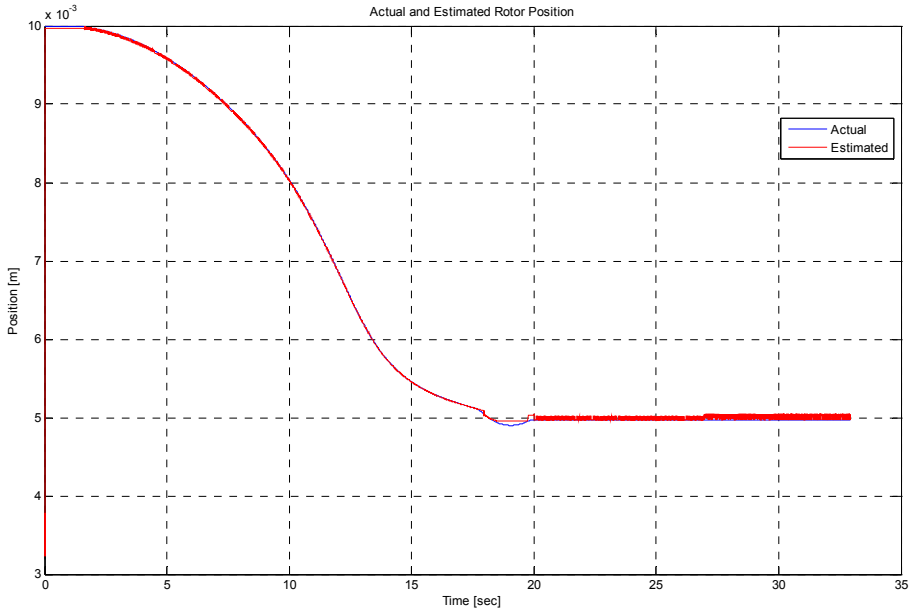

Figure 3-7 Actual and estimated rotor position

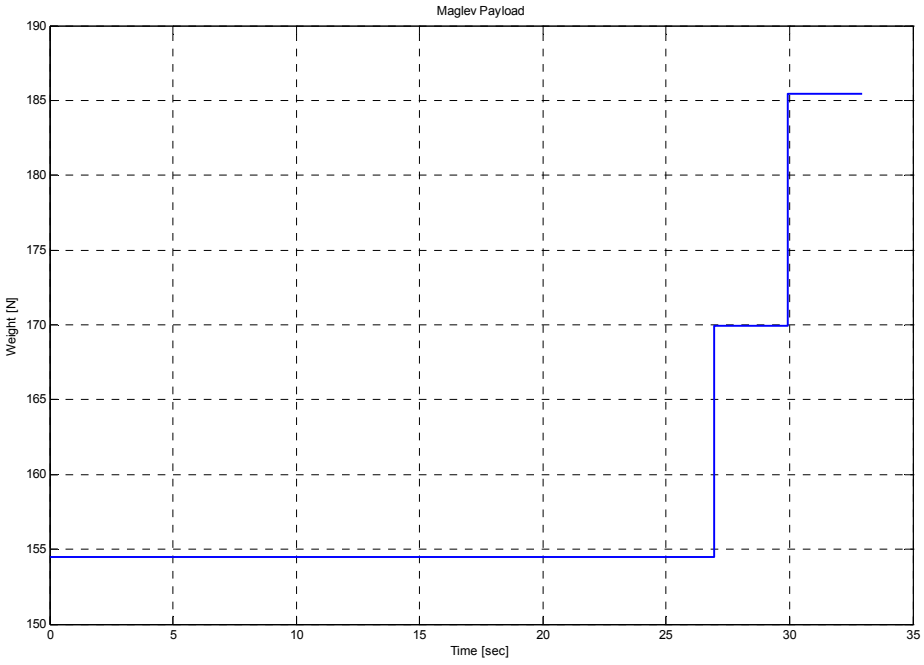

Figure 3-8 Maglev payload variation

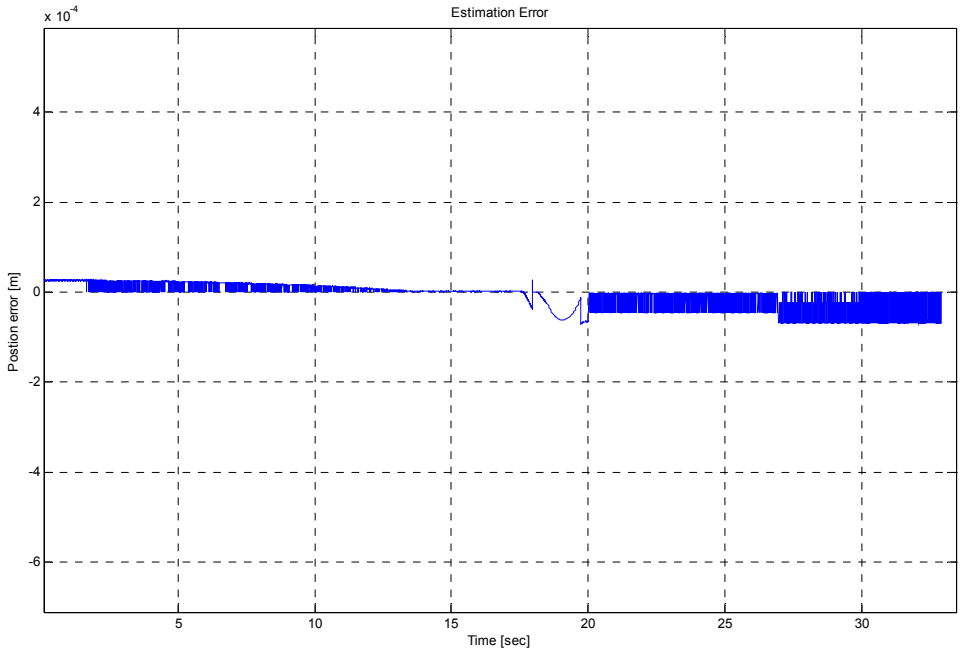

Figure 3-9 Estimation Error

CHAPTER 4

EXPERIMNTAL VERIFICATION OF THE SENSORLESS TECHNIQUE

This chapter provides a description of the maglev hardware used in laboratory experiments. It also deals with implementation issues of the sensorless method by specifying parameters for hardware selection. Experimental results on maglev static parameters are compared with those from the analytical model for model verification. In addition, estimation results are presented for standstill and motion conditions.

4.1 Hardware Description

The laboratory-based maglev system used in this research is shown in Figure 4-1. This maglev system can be regarded as a hybrid EML system where the magnetic attracting forces are produced by the flux in electromagnets and permanent magnets mounted on what we refer to as the rotor. The picture shows the maglev and its parts, namely, stator, rotor, electromagnet coils and Neodymium permanent magnets. Figure 4-2 shows the maglev test bed system architecture. The power source is a 300V DC power supply that is connected to the electromagnet coils through a Semikron power processor that serves as an actuator for coil current control. Figure 4-3 shows a schematic of this connection. The Semikron unit is configured as a full H-bridge for hysteresis current control. The firing of the switches Q1-Q4 is commanded by

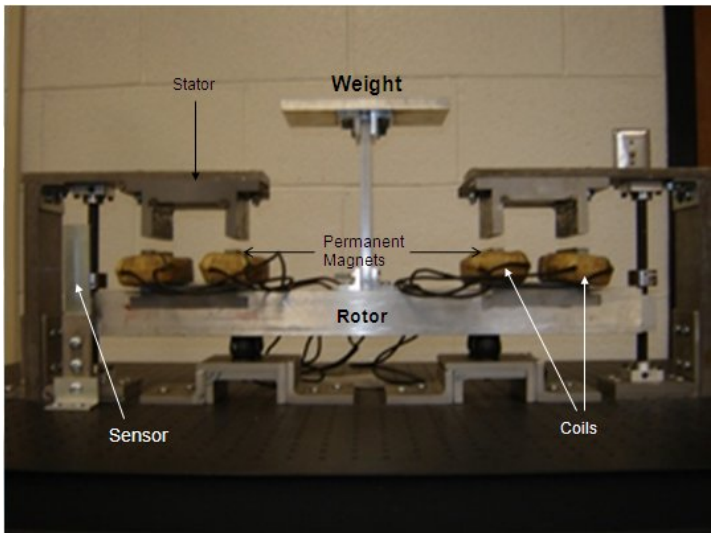

Figure 4-1 The maglev system

a TI TMS320F2812 DSP microcontroller located on the control and signal conditioning board. The proposed sensorless position estimation method uses coil current measurements provided by a hall-effect current sensor. These measurements are the input to the estimation algorithm on the DSP controller where the model-based inductance is used to provide position estimates.

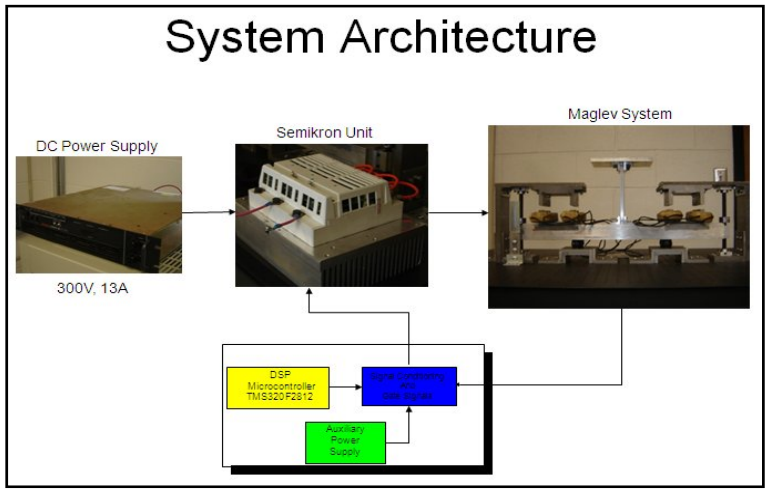

Figure 4-2 Maglev System Architecture

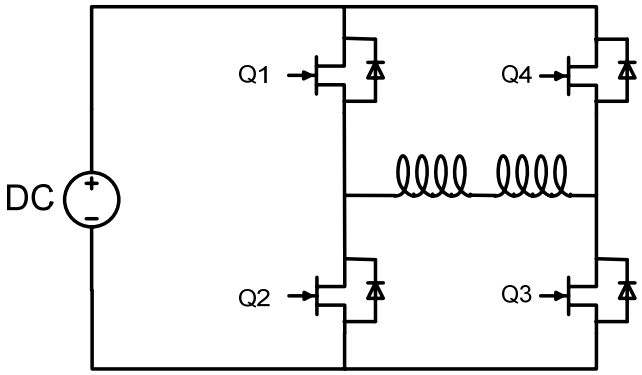

Figure 4-3 Semikron full bridge

The coil current is controlled by actuating the switches in such a way that its value remains within a specified hysteresis band. A positive voltage is applied to the coils if the current value is dropping below a lower limit. On the contrary, if the current is over an upper limit a negative voltage is applied by closing switches Q2 and Q4.

The current sensor output is filtered by a 4th order Butterworth antialiasing filter in a Sallen-Key configuration as shown in figure 4-4.

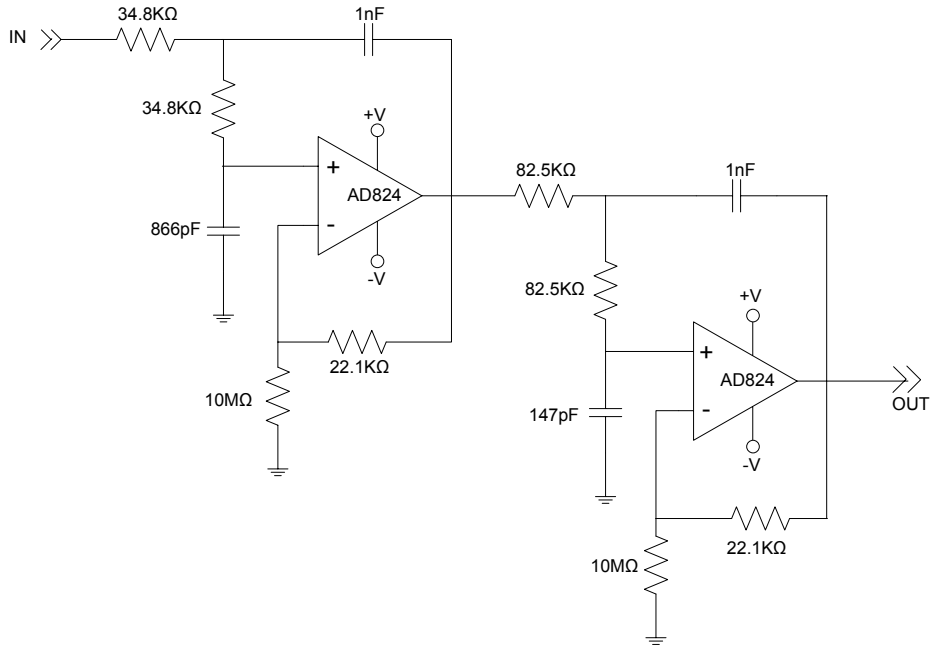

Figure 4-4 4th order Butterworth antialiasing filter

The Butterworth filter was chosen because of its flat characteristics in the pass and stop bands, it is known as a maximally flat filter. The Sallen-Key topology offers the least dependence of filter performance on the performance of the opamp. This is due to the fact that the opamp is not configured as an integrator but rather as an amplifier. The maximum expected switching frequency is around 3.5kHz. The Butterwoth filter has a cutoff frequency of 5Khz. Its frequency response is shown in figure 4-5.

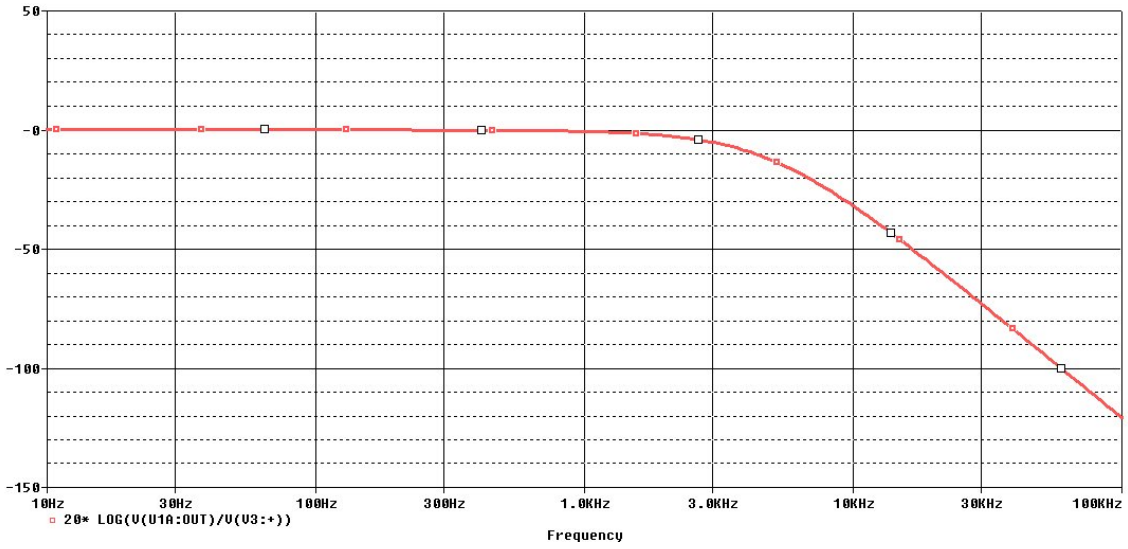

Figure 4-5 Butterworth antialiasing filter magnitude response

4.2 Closed-loop control of current and force

The magnetic attracting force between rotor and stator is given by

$$F_M = \mu_0 A_{Ag} \left[\frac{Ni + H_c L_m}{x + \mu_0 A_{Ag} R_m} \right]^2 = C_1 \left[\frac{Ni + C_2}{x + C_3} \right]^2 \qquad (4.1)$$

Where $C_1=A_g\mu_0$, $C_2=H_cL_m$ and $C_3=\mu_0A_gR_m$. Equation (4.1) suggests that by controlling the coil current the magnetic force can be regulated at any desired value for a given airgap length. The current control is implemented using a hysteresis controller where the value of the current is kept within a desired band by applying maximum and minimum control inputs. In the maglev case that control input is a DC voltage of 300 V. The switching is performed by actuating the switches shown in figure 4-3 according to the logic previously explained in section 4.1 The desired coil current (reference current) is selected by an upper level position controller that process present rotor position information from the estimator and switches the reference current between a minimum and a maximum. It is this coil current that excites the maglev dynamics according to equation (2.16).

The full bridge of figure 4-3 is the actuator for current control. It is important for selection of this module to determine boundaries in switching frequencies. Since the coil current will vary linearly in time, its relation with the applied coil terminal voltage can be expressed according to equation 2.14. The boundaries for switching frequencies can be determined by considering the switches turn-on and turn-off times in figure 4-6.

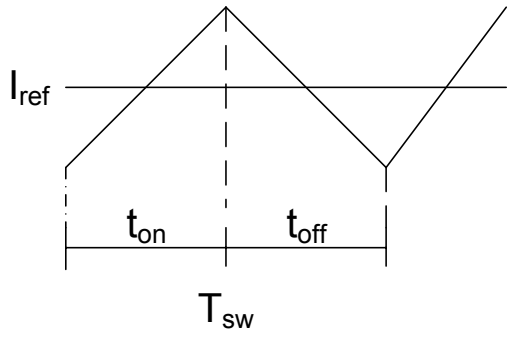

Figure 4-6 Switch turn-on and turn-off times

According to equation 2.14 the turn-on time is given by

$$\Delta t = t_{on} = L(x)\frac{\Delta i}{V} \tag{4.2}$$

The turn-off time is in reality slightly smaller than t_{on} since when applying a negative voltage $-V$ to the circuit the effective voltage seen by the inductor is a little higher (*-V-ri)*. But, a good approximation is to assume *ton = toff* , and therefore the switching period is

$$T_{sw} = t_{on} + t_{off} = 2t_{on} \tag{4.3}$$

The maximum switching frequency must happen when a defined variation of Δi in coil current occurs in the smallest possible time t_{on}. This situation will happen at the minimum value of inductance L_{min} when the airgap length is 10mm. The maximum switching frequency is

$$f_{sw_{max}} = \frac{1}{T_{sw_{min}}} = \frac{1}{2t_{on_{min}}} \tag{4.4}$$

$$f_{sw_{max}} = \frac{V}{2L(x)_{min}\Delta i} = \frac{(x_{max} + H_c L_m) * V}{4N^2 \mu_0 A_m \Delta i} \tag{4.5}$$

An important aspect to point out is how the selection of the hysteresis current band Δi affects the switching frequency. A more strict control imposed on the variation of current will demand faster switching frequencies.

Another parameter of interest is the sampling frequency f_s. In order to control the current, it is necessary to count with at least 2 samples of the coil current, one for the rising current and the other for the falling current, per switching period. In other words, the minimum sampling frequency is given by

$$f_s = 2 * f_{sw_{max}} \tag{4.6}$$

After the geometry of the system has been defined and a suitable hysteresis current band has been selected, the converter switching frequency and sampling frequency can be determined from (4.5) and (4.6). Figure 4-7 is a picture of the coil current (green trace) tracking a reference current of 2A. Figures 4-8 and 4-9 show the coil current variation for a positive and negative current step commands issued by the position controller.

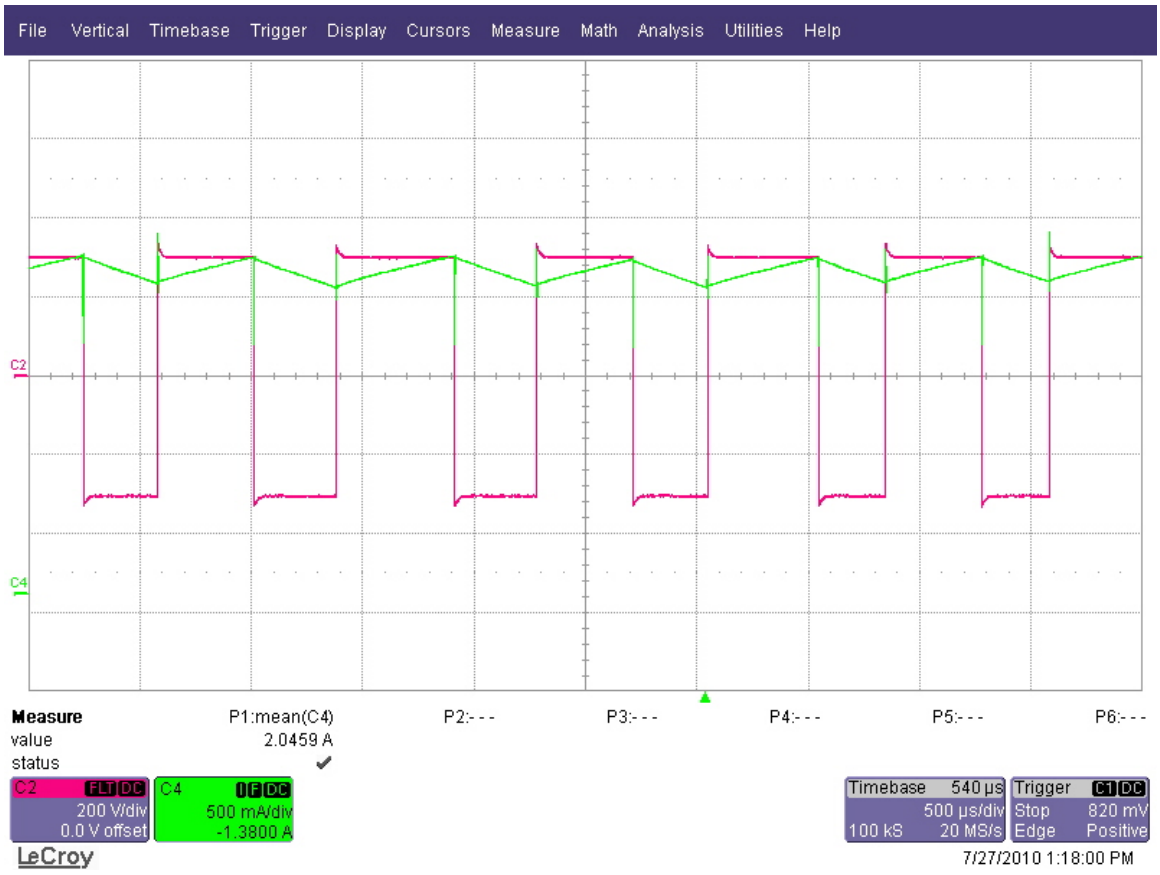

Figure 4-7 Coil current

The red trace is the voltage applied to the coil. The waveform duty cycle is modulated by the current hysteresis controller to achieve current regulation at the reference value. It is seen that even at a reference value as small as 0.1A the controller achieves good current regulation.

Figure 4-8 Positive step command for coil current

Figure 4-9 Negative step command for coil current

A good current control performance is vital for force control. Experimental verification of force generation was carried out by measuring the flux density B_{Ag} in the airgap for several values of current and airgap lengths. These measurements were then used along with the Maxwell Stress Tensor method (equation (2.13)) for force calculation. Table 4-1 list several values of flux density measurements taken at the stator face for a horizontal sweep of 20mm. The corresponding values obtained from FEA analysis are shown in table 4-2. These 2 set of values are plotted in figures 4-10 and 4-11 for airgap lengths of 5 and 10mm respectively. The closeness of experimental and FEA values is evident and served as justification for the use of the FEA model to fine tune the analytical model as it was explained in section 2.4.

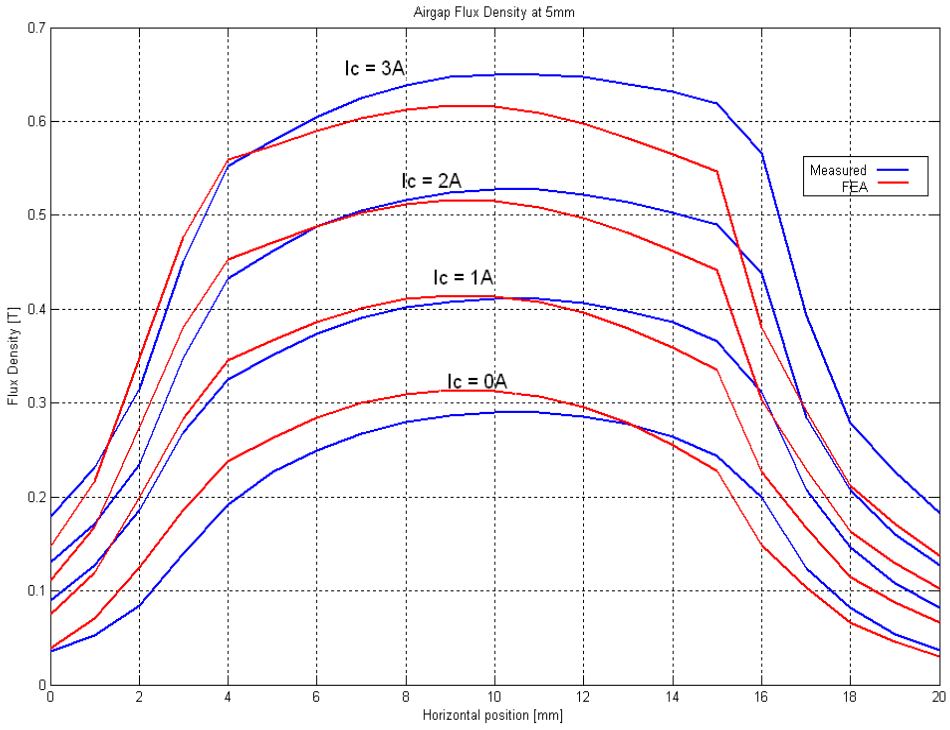

Figure 4-10 Flux density at 5mm airgap length

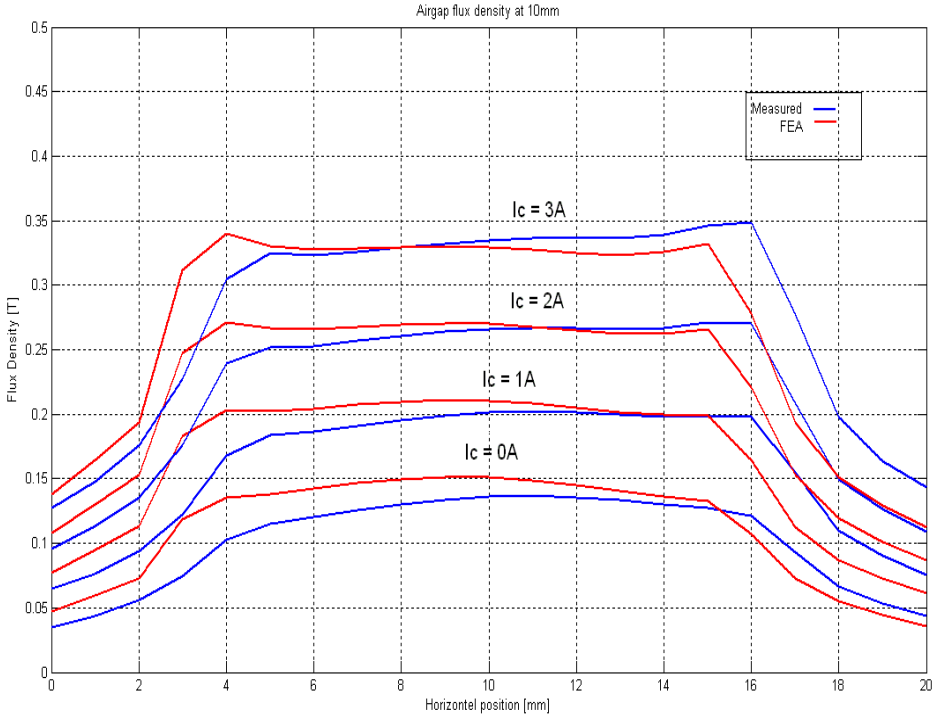

Figure 4-11 Flux density at 10mm airgap length

Although table 4-1 list measurements of flux density for 5 and 10mm, more data was obtained for model verification purposes. Table 4-3 shows the values of forces calculated from measurements of flux density for 5, 6, 7, 8, 9, and 10 mm airgap lengths as well as values of forces obtained from FEA analysis for the same airgap lengths. The difference between them is sometimes negligible and in the worst case within a 11% margin which reflects a good match between the model and the actual system.

Table 4-1 Measured airgap flux density

		Airgap Flux Density [T] Measured Values											
Ag [mm]	I_{coil} [A]	0	1	2	3	4	5	6	7	8	9	10	11
5	0	0.035	0.053	0.084	0.139	0.192	0.227	0.249	0.268	0.280	0.287	0.290	0.290
	1	0.090	0.128	0.186	0.269	0.325	0.351	0.374	0.391	0.402	0.408	0.411	0.411
	2	0.130	0.171	0.234	0.348	0.432	0.462	0.488	0.505	0.516	0.524	0.527	0.527
	3	0.179	0.231	0.315	0.451	0.552	0.580	0.604	0.625	0.638	0.647	0.650	0.650
10	0	0.035	0.044	0.056	0.075	0.102	0.115	0.120	0.126	0.130	0.134	0.136	0.137
	1	0.065	0.077	0.094	0.122	0.168	0.184	0.187	0.191	0.195	0.199	0.201	0.202
	2	0.095	0.113	0.135	0.176	0.239	0.252	0.253	0.257	0.261	0.264	0.266	0.267
	3	0.127	0.148	0.176	0.227	0.305	0.325	0.323	0.326	0.329	0.332	0.335	0.336

Table 4-1 Continued

		Airgap Flux Density [T] Measured Values								
Ag [mm]	I_{coil} [A]	12	13	14	15	16	17	18	19	20
5	0	0.286	0.278	0.264	0.244	0.200	0.124	0.082	0.054	0.036
	1	0.407	0.398	0.386	0.366	0.311	0.207	0.146	0.108	0.082
	2	0.522	0.514	0.503	0.490	0.438	0.284	0.207	0.160	0.127
	3	0.647	0.640	0.632	0.619	0.566	0.393	0.279	0.227	0.183
10	0	0.136	0.133	0.130	0.127	0.121	0.093	0.067	0.053	0.044
	1	0.202	0.200	0.198	0.199	0.198	0.155	0.110	0.090	0.076
	2	0.267	0.266	0.267	0.271	0.270	0.209	0.150	0.127	0.109
	3	0.336	0.336	0.339	0.346	0.349	0.277	0.198	0.164	0.143

Table 4-2 Airgap flux density values from FEA analysis

		Airgap Flux Density [T] Values from FEA analysis											
Ag [mm]	I_{coil} [A]	0	1	2	3	4	5	6	7	8	9	10	11
5	0	0.039	0.070	0.125	0.187	0.238	0.263	0.284	0.300	0.309	0.313	0.313	0.307
	1	0.075	0.119	0.199	0.283	0.345	0.367	0.386	0.401	0.411	0.415	0.414	0.408
	2	0.112	0.168	0.274	0.380	0.453	0.471	0.488	0.502	0.512	0.516	0.515	0.509
	3	0.148	0.217	0.348	0.476	0.560	0.574	0.590	0.603	0.612	0.616	0.615	0.609
10	0	0.047	0.059	0.073	0.119	0.135	0.138	0.143	0.147	0.150	0.151	0.151	0.149
	1	0.078	0.095	0.113	0.183	0.203	0.202	0.204	0.207	0.210	0.211	0.210	0.208
	2	0.108	0.130	0.153	0.247	0.271	0.266	0.266	0.268	0.270	0.271	0.270	0.268
	3	0.138	0.165	0.194	0.311	0.340	0.330	0.328	0.328	0.330	0.330	0.329	0.328

Table 4-2 Continued

		Airgap Flux Density [T] Values from FEA analysis								
Ag [mm]	I_{coil} [A]	12	13	14	15	16	17	18	19	20
5	0	0.296	0.278	0.256	0.228	0.149	0.104	0.066	0.046	0.030
	1	0.397	0.380	0.359	0.335	0.227	0.166	0.115	0.087	0.066
	2	0.498	0.481	0.462	0.441	0.304	0.229	0.163	0.129	0.102
	3	0.598	0.582	0.564	0.547	0.381	0.291	0.212	0.171	0.137
10	0	0.145	0.141	0.136	0.133	0.107	0.073	0.055	0.044	0.036
	1	0.205	0.202	0.199	0.199	0.164	0.113	0.087	0.073	0.061
	2	0.265	0.262	0.262	0.265	0.221	0.153	0.119	0.101	0.087
	3	0.325	0.323	0.325	0.332	0.278	0.193	0.152	0.130	0.112

Table 4-3 Maglev magnetic force

		FEA analysis	From measurements
Ag [mm]	Ic [A]	Force [N]	Force [N]
5	0	86.153	75.683
	1	166.531	170.213
	2	273.794	290.955
	3	407.461	461.145
6	0	63.417	53.080
	1	125.297	120.073
	2	208.562	211.095
	3	312.887	336.524
7	0	48.144	41.003
	1	97.154	92.717
	2	163.585	166.502
	3	247.234	265.547
8	0	37.535	30.967
	1	77.289	71.592
	2	131.531	129.441
	3	200.138	208.400
9	0	29.846	24.801
	1	62.659	58.464
	2	107.706	106.644
	3	164.920	172.554

Table 4-3 Continued

		FEA analysis	From measurements
Ag [mm]	Ic [A]	Force [N]	Force [N]
10	0	24.144	19.383
	1	51.6329911	46.449
	2	89.593	85.32659918
	3	137.983	138.963

4.3 Estimation of airgap length at standstill

Equations (3.4) and (3.5) were used for online calculation of inductance at standstill and estimation of the airgap length. Figure 4-12 shows the frequency histograms of the estimated airgap lengths for 5, 6, 7 and 8mm. These histograms reflect what it was previously seen from the sensitivity analysis, i.e., the proportional change in inductance is larger for smaller airgap lengths and therefore it is easier to discriminate between their values. This larger difference between inductance values facilitates the estimation of smaller airgaps which is an advantageous feature. Table 4-4 lists some of the statistical measures for these estimates. These measures show that the proposed estimation method performs very well at standstill.

Table 4-4 Airgap estimate statistics

Airgap length [mm]	Mean [mm]	σ [mm]	σ^2 [mm^2]
5	4.9	0.1304	0.0170

Table 4-4 Continued

Airgap length [mm]	Mean [mm]	σ [mm]	σ^2 [mm^2]
6	5.9	0.1644	0.0270
7	6.9	0.1326	0.0176
8	8.2	0.1273	0.0162
9	8.9	0.1783	0.0318
10	10.4	0.2446	0.0598

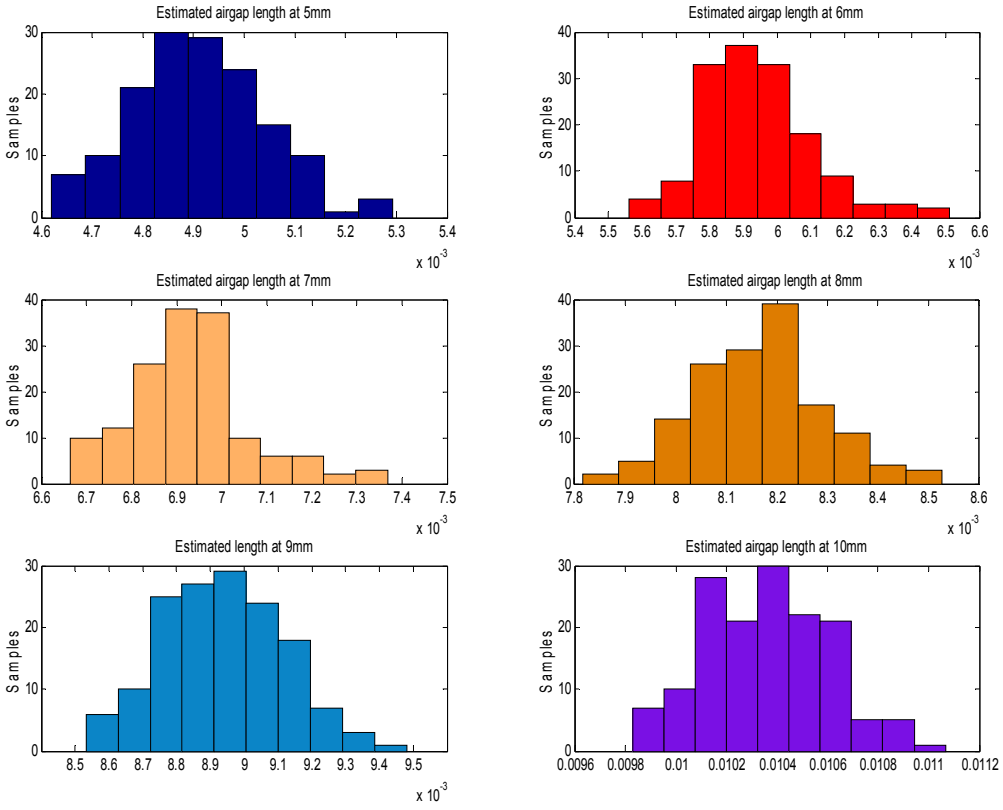

Figure 4-12 Estimated airgap length histograms

4.4 Estimation of airgap length during motion

The estimation of airgap length in motion is performed using the same equations ((3.4) and (3.5)) as before, since the assumption of a negligible speed variation between current transitions still holds for slow rotor speeds. Figure 4-13 shows the rotor position estimates during motion as well as the actual or measured position (blue trace). The results show once again that the estimation method performs better for smaller airgap lengths. As seen in the figure the tracking of the measured position values becomes better towards the end of the test when the rotor is getting closer to the reference airgap length of 5mm. As the rotor gets closer to the stator, the airgap reluctance decreases and the proportional change in flux linkage increases causing an increase in inductance. These larger changes in inductances suit the estimation process.

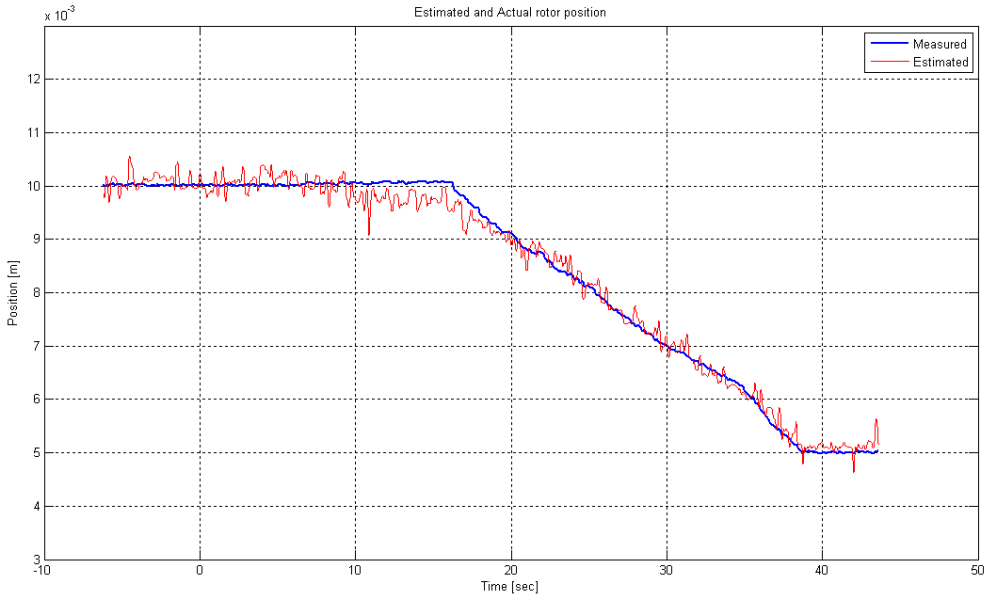

Figure 4-13 Estimated and actual rotor position

The rotor position estimation error is shown in figure 4-14. This error presents a mean of 0.0154mm, a standard deviation of 0.205mm and a variance of 0.0419mm^2. According to figure 4-14, most estimation error values are within the ±3σ band, which grants the method a good sense of accuracy. This characteristic can also be identified in figure 4-15 where a histogram of the estimation error distribution is shown. The figure show a high density around the mean and it is clear that most of the values are within the ±0.6mm band. This band might seem a little large, but in maglev transportation applications, like the German Transrapid system, the operating tolerances between the guideway and vehicle are around 2mm [18] which makes this method a very well suited technology for maglev transportation systems.

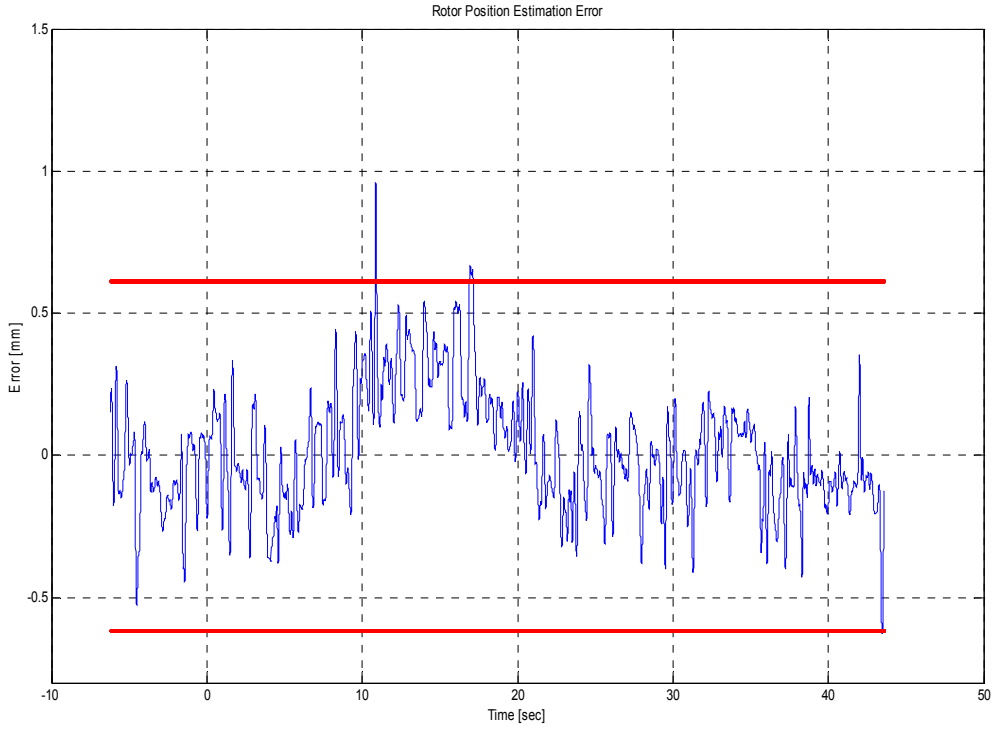

Figure 4-14 Position estimation error

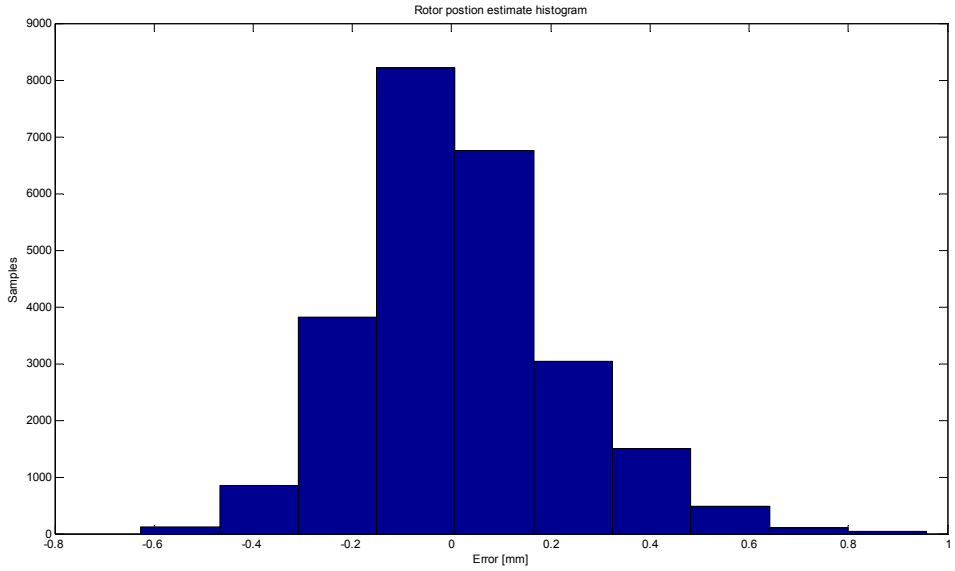

Figure 4-15 Position estimation error histogram

4.5 Discussion of the results

Measured static parameters of the maglev system have been compared with analytical results that show a good match between experimental measurements and the maglev analytical model. The closeness in measured force values and analytical values provided a justification for using the analytical model as a reliable means for research. The model provided valuable information regarding variation of static parameters like inductance and its relation to rotor position. Force-current characterization determined the maximum coil current as an input to the maglev dynamics.

The sensorless technique proved to be a viable technology for maglev systems. The results show that the method provides estimates with an accuracy of 0.6mm in motion conditions and 0.3mm at the desired airgap length that suits very well maglev applications.

The range in inductance variation was found to be very small. The estimation method could benefit of a larger range of inductance variation by changing the geometry of the stator-rotor pair. A change in geometry that decreases the effective reluctance of the airgap will yield larger changes in inductance, and therefore render better accuracy.

CHAPTER 5

CONCLUSIONS AND FUTURE RESEARCH

5.1 Conclusions

In this research, a position sensorless estimation method for maglev applications was studied and implemented on a laboratory –based maglev system with one degree of freedom. The method takes advantage of a position dependent magnetic signature of the system, namely, its inductance to make on-line estimates of the levitated object's position. The method proved to be accurate enough for maglev applications like transportation systems where the operating tolerances can be met by the proposed method's accuracy.

This sensorless approach showed low sensitivity to abnormal geometrical changes (rotor-stator misalignments). This is due to the fact that the system inductance is not majorly affected by geometrical changes that effectively increase the airgap reluctance. However, the system inductance presents a significant change when this reluctance is reduced. This fact can be used to improve the estimation accuracy. One way to reduce the airgap reluctance is by increasing its cross-sectional area. A wider rotor/stator pole face will reduced the reluctance and decrease flux leakage. This increase in flux linkange will cause an increase in inductance and will make it even more sensitive to changes in reluctance at large and small airgap lengths. As a result, the sesnsorless approach will have more accuracy than the one observed in the present system.

There are several aspects to consider for implementation of the sensorless method. Among other parameters, switching frequency is an important parameter to observe when selecting the power converter. A boundary for the maximum switching frequency has been provided in terms of other system parameters. DC bus voltage, hysteresis current band, permanent magnet reluctance, coil turns, among others, are the factors that affect the switching frequency. Ultimately, all of them relate to the system inductance.

The importance of having a good regulation of airgap length in maglev transportation systems resides in the fact that ride quality and optimal production of thrust force are directly affected by the airgap between the guideway and vehicle. The position sensorless estimation approach presented in this work can improve the reliability of current systems by providing a fall-back strategy in case of sensor failure. In addition, it can serve as the main provider of position information in applications where the installation of an electromechanical sensor is not viable.

The sensorlesss approach provides a relatively simple but insightful option to other parameter estimation methods. The estimates where obtain without the need of process noise characterization which in other approaches are sometimes cumbersome to realize. The only requirement for the implementation of the proposed estimation approach is a set of terminal measurements that in any case would have to be accessible for control purposes and therefore there is no need for additional hardware.

5.2 Future research

One of the main assumptions that this approach drew upon was that the rotor speed does not significantly change between coil current transitions. A more general approach will consider a solution for higher rotor speeds.

The study of ride quality and resonance due to guideway oscillation are important aspects of maglev transportation applications. A study of these phenomena and its impact in sensorless approaches will grant a broader understanding of the capabilities of the sensorless method.

Bang-bang controllers of higher complexity have been reported for other maglev applications. These controllers required information on not only position but also speed. The performance of the sensorless estimation method could also be explored with these types of controllers, where the speed information would have to be inferred from position estimates.

REFERENCES

[1]. Nagaya, K. and M. Ishikawa, *A noncontact permanent magnet levitation table with electromagnetic control and its vibration isolation method using direct disturbance cancellation combining optimal regulators.* Magnetics, IEEE Transactions on, 1995. **31**(1): p. 885-896.

[2]. Bleuler, H., *A survey of magnetic levitation and magnetic bearing types.* International Journal of Japan Society of Mechanical Engineers, 1992(35): p. 335-342.

[3]. Verma, S., K. Won-jong, and G. Jie, *Six-axis nanopositioning device with precision magnetic levitation technology.* Mechatronics, IEEE/ASME Transactions on, 2004. **9**(2): p. 384-391.

[4]. Jacobs, W.A., *Magnetic launch assist-NASA's vision for the future.* Magnetics, IEEE Transactions on, 2001. **37**(1): p. 55-57.

[5]. El Hajjaji, A. and M. Ouladsine, *Modeling and nonlinear control of magnetic levitation systems.* Industrial Electronics, IEEE Transactions on, 2001. **48**(4): p. 831-838.

[6]. Feifei, Z. and K. Suyama. *Nonlinear feedback control of magnetic levitating system by exact linearization approach*. in *Control Applications, 1995., Proceedings of the 4th IEEE Conference on*. 1995.

[7]. Filho, M.R. and C.J. Munaro. *A design methodology of tracking controllers for magnetic levitation systems*. in *Control Applications, 2001. (CCA '01). Proceedings of the 2001 IEEE International Conference on*. 2001.

[8]. Al-Muthairi, N.F. and M. Zribi, *Sliding Mode Control of a Magnetic Levitation System.* Mathematical Problems in Engineering, 2004. **2004**(2): p. 93-107.

[9]. Faa-Jeng, L., et al., *Hybrid controller with recurrent neural network for magnetic levitation system.* Magnetics, IEEE Transactions on, 2005. **41**(7): p. 2260-2269.

[10]. Taghavi-Zargar, O., *Fuzzy Logic control of a Magnetically Levitated System with Hardware implementation*, in *Mechanical Engineering*. 2001, University of Texas at Arlington: Arlington.

[11]. Munaro, C.J., et al. *Modeling and observer-based nonlinear control of a magnetic levitation system*. in *Control Applications, 2002. Proceedings of the 2002 International Conference on*. 2002.

[12]. Henley, J.A., *Design and Implementation of a Feedback Linearizing Controller and Kalman Filter for a Magnetic Levitation System*, in *Mechanical Engineering*. 2007, University of Texas at Arlington: Arlington.

[13]. Moon, F.C., *Superconducting Levitation: Aplications to Bearings and Magnetic Transportation*. Second ed. 1993, New York: John Wiley & Sons, Inc. 295.

[14]. Bianchi, N., *Permanet Magnets Synchronous Motors*, in *Hanbook of Power Electronics*. 2010.
[15]. Fahimi, B. *Qualitative approach to electromechanical energy conversion: Reinventing the art of design in adjustable speed drives*. in *Electrical Machines and Systems, 2007. ICEMS. International Conference on*. 2007.
[16]. Sinha, P.K., *Electromagnetic Suspension: Dynamics and Control*. IEE Control Engineering, ed. D.P. Atherton. Vol. 30. 1987, London: Peter Peregrinus Ltd.
[17]. Fahimi, B., A. Emadi, and B. Sepe, Jr., *Position sensorless control.* Industry Applications Magazine, IEEE, 2004. **10**(1): p. 40-47.
[18]. Film, P.; Available from: http://www.parallaxfilm.com/promo/maglev/.
[19]. Slotine, J.E. and W. Li, *Applied Nonlinear Control*. 1991, Upper Saddle River: Prentice Hall.
[20]. Suresh, G., B. Fahimi, and M. Ehsani. *Improvement of the accuracy and speed range in sensorless control of switched reluctance motors*. in *Applied Power Electronics Conference and Exposition, 1998. APEC '98. Conference Proceedings 1998., Thirteenth Annual*. 1998.
[21]. Suresh, G., et al. *Inductance based position encoding for sensorless SRM drives*. in *Power Electronics Specialists Conference, 1999. PESC 99. 30th Annual IEEE*. 1999.
[22]. Xin, K., Q. Zhan, and J. Luo. *A new simple sensorless control method for switched reluctance motor drives*. in *Electrical Machines and Systems, 2005. ICEMS 2005. Proceedings of the Eighth International Conference on*. 2005.
[23]. G. Serdar Tombul, S.P.B., Nizami Akturk, *Sliding mode control for a class of non-affine nonlinear systems.* Nonlinear Analysis, 2009. **71**: p. e1589-e1597.
[24]. Kaloust, J., et al., *Nonlinear robust control design for levitation and propulsion of a maglev system.* Control Theory and Applications, IEE Proceedings -, 2004. **151**(4): p. 460-464.
[25]. Boukhobza, T.K., L., *Sliding-mode control for nonlinear systrems non affine in the input*, in *AFOSR Workshop and Contractors' Meeting: Dynamics and Control* 2004: Pasadena, California.

BIOGRAPHICAL INFORMATION

Esteban R. Noboa was born on June 9, 1972 in Guayaquil, Ecuador. He received his Bachelor of Science in Electrical Engineering from Escuela Superior Politecnica del Litoral, Guayaquil, Ecuador in 1999. On graduation he was recruited by Emelgur S. A. utility company in Guayaquil where he worked for two years. In his role as an electronic engineer he participated in the development of a Supervisory and Data Acquisition (SCADA) System for the control of 23 power substations deployed in rural areas. In fall 2001 he started his graduate program in Electrical Engineering at the University of Texas at Arlington. He received his Master of Science degree in Electrical Engineering from The University of Texas at Arlington in summer 2003. In fall 2003 he started his Doctorate program in Electrical Engineering at The University of Texas at Arlington. In Fall 2010 he received his PhD in Electrical Engineering from The University of Texas at Arlington. Esteban's research interests include magnetic suspension systems, control of power converters and integration of renewable energy sources.